Stoichiometry of Nck-dependent actin polymerization in living cells

Jonathon A. Ditlev,[1,2] Paul J. Michalski,[2] Greg Huber,[2] Gonzalo M. Rivera,[3] William A. Mohler,[1,2] Leslie M. Loew,[2] and Bruce J. Mayer[1,2]

[1]Department of Genetics and Developmental Biology, Raymond and Beverly Sackler Laboratory of Genetics and Molecular Medicine, and [2]Richard D. Berlin Center for Cell Analysis & Modeling, University of Connecticut Health Center, Farmington, CT 06030
[3]Department of Pathobiology, Texas A&M University, College Station, TX 77843

Regulation of actin dynamics through the Nck/N-WASp (neural Wiskott–Aldrich syndrome protein)/Arp2/3 pathway is essential for organogenesis, cell invasiveness, and pathogen infection. Although many of the proteins involved in this pathway are known, the detailed mechanism by which it functions remains undetermined. To examine the signaling mechanism, we used a two-pronged strategy involving computational modeling and quantitative experimentation. We developed predictions for Nck-dependent actin polymerization using the Virtual Cell software system. In addition, we used antibody-induced aggregation of membrane-targeted Nck SH3 domains to test these predictions and to determine how the number of molecules in Nck aggregates and the density of aggregates affected localized actin polymerization in living cells. Our results indicate that the density of Nck molecules in aggregates is a critical determinant of actin polymerization. Furthermore, results from both computational simulations and experimentation support a model in which the Nck/N-WASp/Arp2/3 stoichiometry is 4:2:1. These results provide new insight into activities involving localized actin polymerization, including tumor cell invasion, microbial pathogenesis, and T cell activation.

Introduction

Signal-directed cytoskeletal rearrangements are required for many essential cellular processes, including adhesion, migration, and vesicle trafficking (Pollard and Borisy, 2003). Tyrosine phosphorylation is an important mechanism regulating actin remodeling (Pawson, 2004). Recruitment of the Nck family of Src homology (SH) 2/SH3 domain–containing adaptor proteins to phosphotyrosine residues induces cytoskeletal changes through the recruitment and activation of the Wiskott–Aldrich syndrome protein (WASp) or neural WASp (N-WASp)–Arp2/3 complex pathway. The involvement of this pathway in axon guidance (Rao and Zipursky, 1998; Rao, 2005), maintenance of the glomerular filtration barrier (Jones et al., 2006, 2009; Verma et al., 2006; Bertuccio et al., 2011), T cell activation (Barda-Saad et al., 2005, 2010; Jordan et al., 2006; Pauker and Barda-Saad, 2011), and invasion of cancer cells (Yamaguchi et al., 2005; Lapetina et al., 2009; Stylli et al., 2009; Oser et al., 2010, 2011) has been well documented.

Previous studies have demonstrated that N-WASp integrates signals from multiple sources, including the Rho family GTPases, phosphoinositides, and SH2/SH3 domain–containing adaptor proteins (Carlier et al., 2000; Moreau et al., 2000; Prehoda et al., 2000; Fukuoka et al., 2001; Rivera et al., 2009; Padrick and Rosen, 2010). Combinatorial binding of these upstream signaling molecules increases N-WASp activity, which, in turn, stimulates localized actin polymerization (Rohatgi et al., 2001; Papayannopoulos et al., 2005).

The actin cytoskeleton is a highly dynamic network controlled by multiple regulatory mechanisms (dos Remedios et al., 2003; Pollard, 2007). Because of the complexity of the system, experimental investigations into the specific roles of individual modulators and pathways have proven difficult to interpret. To address these experimental limitations, computational modeling has been used for the comprehensive testing and prediction of the effects of a variety of perturbations on cytoskeletal dynamics

Correspondence to Bruce J. Mayer: bmayer@neuron.uchc.edu; or Leslie M. Loew: les@volt.uchc.edu

Abbreviations used in this paper: AU, arbitrary unit; KO, knockout; MEF, mouse embryonic fibroblast; N-WASp, neural WASp; SH, Src homology; WASp, Wiskott–Aldrich syndrome protein; WIP, WASp-interacting protein; WT, wild type.

The Rockefeller University Press $30.00
J. Cell Biol. Vol. 197 No. 5 643–658
www.jcb.org/cgi/doi/10.1083/jcb.201111113

(Alberts and Odell, 2004; Bindschadler et al., 2004; Carlsson et al., 2004; Carlsson, 2006; Mogilner, 2006; Beltzner and Pollard, 2008; Novak et al., 2008; Ditlev et al., 2009; Michalski and Carlsson, 2010).

We have previously demonstrated that clustering of membrane-targeted Nck SH3 domains induces actin polymerization in the form of highly motile actin comet tails (Rivera et al., 2004, 2009). We have also created a computational model of the actin cytoskeleton (Ditlev et al., 2009; Kapustina et al., 2010). In this study, we introduced modifications to these tools to examine the quantitative relationships between Nck and actin dynamics. Through a combination of quantitative experimentation, fluorescence imaging, and computational modeling, we demonstrate that as the local density of Nck SH3 domains increases, actin polymerization increases in a nonlinear manner. Computational predictions and experimental results strongly suggest that the nonlinear dependence of actin polymerization on Nck density is the result of a previously unappreciated 4:2:1 Nck/N-WASp/Arp2/3 mechanistic stoichiometry.

Results

The number of Nck molecules in aggregates and velocity of aggregates do not independently predict characteristics of actin comet tails

Antibody-induced aggregation of membrane-bound Nck SH3 domains has been shown to induce the formation of robust actin comet tails via activation of N-WASp and the Arp2/3 complex (Rivera et al., 2004). As in Rivera et al. (2004), Nck SH3 domains fused to a transmembrane CD7 domain and an extracellular CD16 domain were aggregated using primary anti-CD16 monoclonal antibodies and secondary anti–mouse IgG (Fig. S1 A). After incubation with primary and secondary antibodies, fluorescently labeled Nck SH3 aggregates and fluorescently labeled actin were visualized using time-lapse confocal microscopy (see Materials and methods for more details).

Using this experimental approach, we quantified the relationship between Nck aggregate properties and the resulting effects on the actin cytoskeleton. An advantage of this approach is that both the signal input (Nck aggregation) and output (actin polymerization) can be precisely quantified. Measurement of the number of molecules in individual aggregates was accomplished by imaging membrane-bound Nck SH3 domains fluorescently tagged with mCherry. Aggregation of mCherry–Nck SH3 molecules resulted in the formation of robust, motile actin comet tails (Fig. 1 [A and B] and Video 1), similar to those seen in previously published studies using unlabeled Nck constructs (Rivera et al., 2004, 2009). From these images, the number of molecules in aggregates and the velocity of aggregates were measured. The length, peak actin concentration, distance between aggregate centroid and peak actin concentration, and total number of actin molecules in the comet tail core (the central voxels from the beginning to the end of the imaged comet tail) were also measured (see Materials and methods for details).

Because antibody-induced Nck SH3 clusters occur in a broad range of sizes and the velocities of the resultant actin comets are also distributed in a broad range, this system allowed us to examine the quantitative relationships between Nck aggregate size, aggregate velocity, and F-actin distribution in vivo. We first compared the number of Nck molecules in aggregates with the translational velocity of aggregates, which should depend on the rate of filament elongation (Fig. 1 C). We found that aggregates containing similar numbers of Nck molecules were propelled across the membrane at a wide range of velocities; likewise, aggregates traveling at similar velocities could be composed of any number of Nck molecules. These data suggest that size and velocity are independent properties of individual aggregates and, therefore, are not predictive of one another.

We then looked for separate relationships between actin comet tail characteristics and aggregate size or comet velocity (Fig. S2, A and B). In no instance was a strong correlation observed (Pearson correlation coefficients ranging from −0.051 to 0.510). Moderate correlation was seen in several cases, however; for example, total actin molecules in the comet tail were positively correlated with the number of Nck molecules in the aggregate, and peak actin concentration showed a weak negative correlation with aggregate velocity. Overall, quantitative analysis suggests that neither aggregate size nor velocity alone is sufficient to predict actin comet tail characteristics.

Experimentally measured Nck SH3 aggregate size and velocity, together, are predictive of actin comet tail characteristics

To further examine the relationship between Nck SH3 aggregates and actin polymerization—more specifically, whether aggregate size and velocity can be used in concert to predict actin polymerization downstream of Nck aggregates—an optimized version of our model of actin dendritic nucleation (Ditlev et al., 2009; Kapustina et al., 2010) was used to simulate the aggregate/actin comet tail system (Fig. 2 A and Tables S2–S4; also see Methods and materials). Use of this model allowed us to quantitatively compare biochemical model predictions with experimentally measured in vivo data. Partial differential equation simulations were run using a 2D geometry comprised of 2,142 mesh elements (25.0 µm × 14.0 µm, 153 × 14 mesh units), which matched the X-Z pixel sizes of confocal images used in aggregate and comet tail visualization. Nck SH3 molecules were localized to a patch on the membrane of the simulation space (Fig. 2 B). Based on the molecular size of the CD16 structure, which has a diameter of ∼5 nm (Sondermann et al., 2000), the density of molecules within a tightly packed aggregate was estimated to be 25,000 molecules/µm^2. To verify this approximation, we used this estimated density along with the total number of molecules in an aggregate (obtained from the total fluorescence intensity) to predict the size of 33 aggregates. The physical sizes of these aggregates were then directly determined using the distance between the half-maximum intensity on each side of the aggregate to account for the point spread function of the fluorescence. In all cases, the estimated size agreed with the measured size to within 7%.

In our model, Nck recruits and activates N-WASp, which in turn binds and activates the Arp2/3 complex, inducing localized

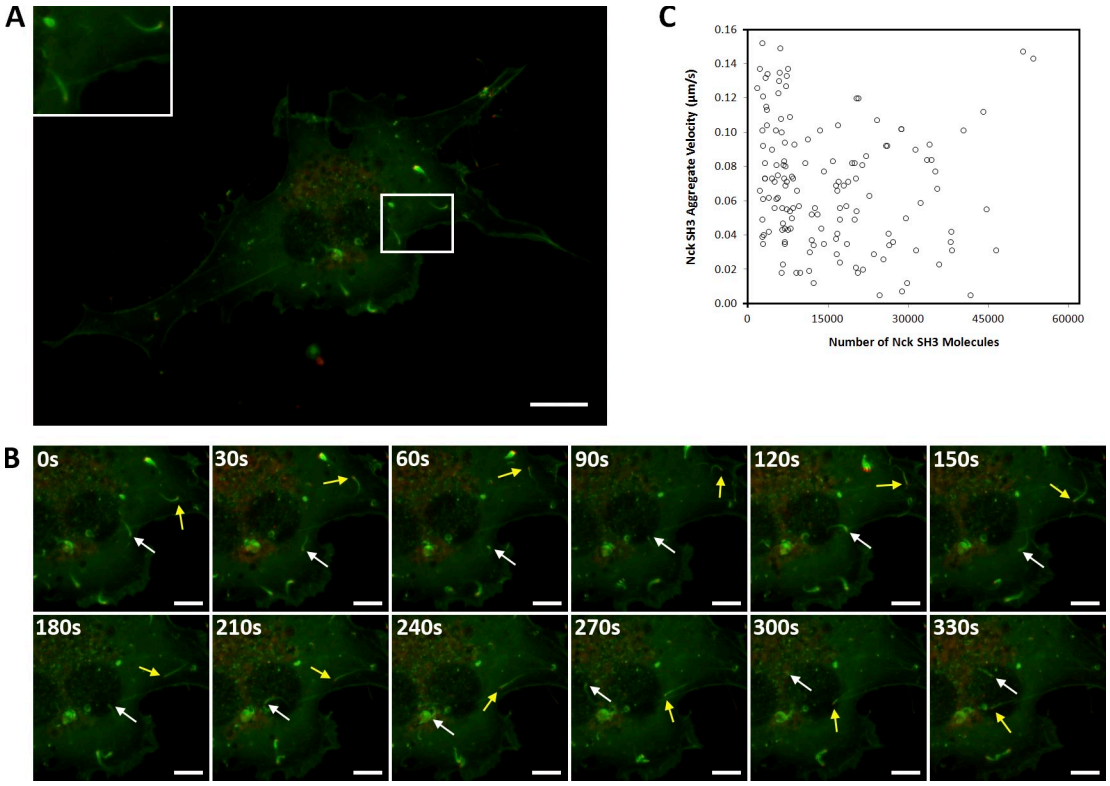

Figure 1. **Aggregation of CD16/7-mCherry–Nck SH3 domains induces actin comet tails.** (A) Representative confocal image of an NIH-3T3 cell cotransfected with GFP-actin and CD16/7-mCherry–Nck SH3 domains. Antibody-induced aggregation of Nck SH3 domains results in robust actin comet tails. A higher magnification of clusters is shown in the inset. Bar, 10 µm. (B) Time-lapse confocal images of two representative (n = 145) aggregate/actin comet tails (white and yellow arrows) demonstrate aggregate motility. Images were taken at 30-s intervals over the course of 4.5 min. Bars, 1 µm. (C) Quantitative analysis of individual actin comets. A plot of Nck SH3 molecules in aggregate versus aggregate velocity (n = 145) shows no apparent correlation.

actin nucleation and polymerization at the Nck SH3 cluster. After Arp2/3 complex activation and branch formation, N-WASp dissociates from the branch, allowing the branch to be released into the cytosol. Branches could then dissociate from ATP- or ADP-P_i–bound mother filament subunits at a rate of 0.04 s^{-1} or from ADP-bound mother filament subunits at a rate of 0.2 s^{-1} (Mahaffy and Pollard, 2006). Advection of all cytosolic molecules was used to represent aggregate velocity; this corresponds to a moving frame of reference centered on the Nck SH3 cluster. Simulations were run using five different aggregate sizes (corresponding to 6,000, 10,000, 17,000, 25,000, and 34,000 Nck molecules when extrapolated to three dimensions) and five aggregate velocities (0.025, 0.050, 0.075, 0.100, and 0.125 µm/s), spanning the range of measured values for these experimental variables. It is important to note that our model does not include parameters that describe forces acting on the aggregate/comet tail system; however, we would predict that existing forces would have little effect on our modeling databased on results examining the force–velocity relationship in actin-based propulsion (McGrath et al., 2003; Wiesner et al., 2003).

Model predictions of actin distribution in comet tails were consistent with averaged experimental data (n = 2–9 aggregates, depending on experimental data available within bins centered on the selected parameter values) when the aggregate size was varied in different simulations at a given velocity (Fig. 2 C). Each increase in aggregate size led to an increase in the peak actin concentration as well as an increase in the amount of actin in the comet tail core. However, the dependence of peak actin concentration on aggregate size is weak, with a sixfold increase in Nck aggregate size resulting in only a twofold increase in actin. Comparisons of actin comet tail characteristics in aggregates with similar size but differing velocities were also consistent between the model and averaged experimental results (n = 2–11 aggregates; Fig. 2 D). Increased aggregate velocity resulted in decreased peak actin concentration and increased centroid-to–peak actin distance, both for simulated and experimentally measured actin comet tails induced by aggregates of varying size. As can be appreciated based on these results, the actin comet tail characteristics depend on both the size and velocity of Nck SH3 clusters.

To further probe the consistency between predicted and averaged experimental comet tails, individual actin comet tails were simulated using experimentally measured aggregate sizes and velocities. This tests the ability of the Virtual Cell model to accurately predict the actin polymerization induced by an experimentally measured aggregate rather than an averaged set of experimental data. Multiple simulations were run using a variety of aggregate sizes and velocities corresponding to individual experimentally analyzed Nck SH3 cluster–induced actin comets. Fig. 2 E shows four typical examples out of 145 individual analyses and illustrates a representative comparison between a predicted and an experimental actin comet tail. The linescans of the actin profiles from both predicted and experimental actin comet tails were similar, despite a modest but consistent

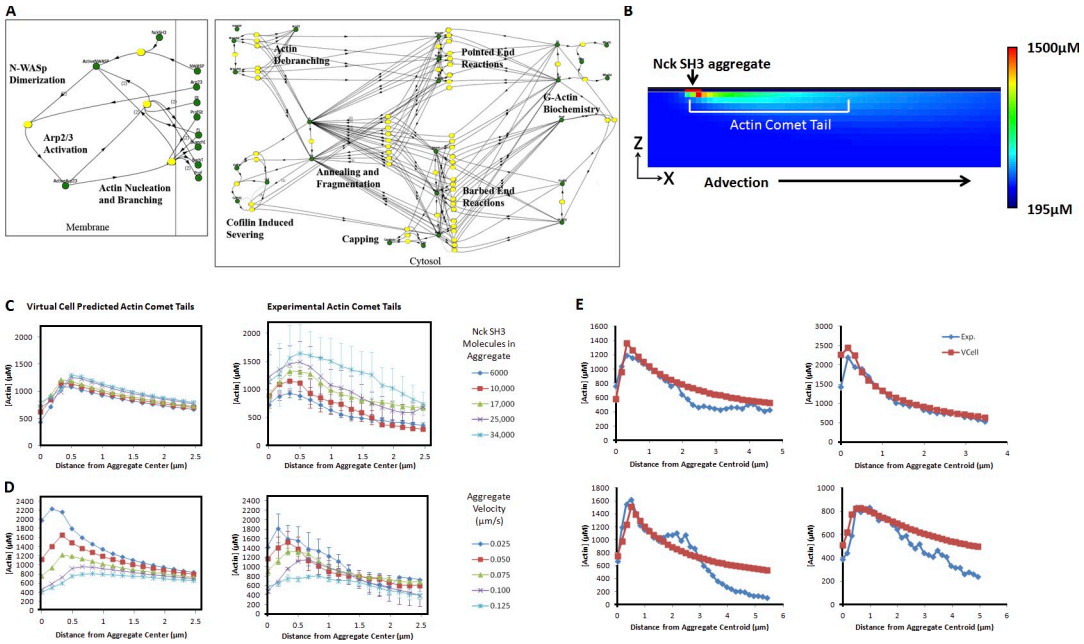

Figure 2. **The Virtual Cell predicts experimental actin comet tail characteristics at steady state if aggregate size and velocity are known.** We adapted a previously published Virtual Cell model to our experimental system to test the theoretical effect of aggregate size and velocity on actin polymerization. Using this model, we show that when aggregate size and velocity are known, actin polymerization downstream of Nck SH3 aggregates can be predicted. (A) Virtual Cell reaction diagram of the simplified actin dendritic nucleation model in which N-WASp is activated on the membrane by Nck. In the Virtual Cell reaction diagram, green circles represent species that participate in reaction, yellow ovals represent biochemical reactions, lines connecting species and reactions indicate the reactants and products of each reaction, and the vertical line in the left schematic designates the separation between membrane and cytosol. The reaction scheme on the left describes membrane reactions, whereas the reaction scheme on the right describes cytosolic reactions. The detailed schematic can be found in the Virtual Cell database under the user JDitlev, model Nck Induces Actin Comet Tail Formation Single NWASP Activation of Arp2/3 Simplified Actin Dendritic Nucleation. (B) Example of an Nck-induced actin comet tail from Virtual Cell simulations at steady state. Nck SH3 domains were localized to a patch on the membrane (red membrane mesh units) inducing actin polymerization in the adjacent mesh units in the cytosol (scaled from blue ∼195 μM to red ∼1,500 μM). Actin then flowed away from the Nck SH3 patch, as indicated by the advection arrow, at a constant velocity to mimic actin propulsion of the Nck SH3 aggregate. (C) Predicted versus experimental actin comet tails induced by aggregates traveling at similar velocities (0.060–0.090 μm/s). Experimental data were divided into five groups by aggregate size (n = 2–9). The mean experimentally measured actin concentrations from linescans were compared with Virtual Cell predictions. Virtual Cell simulations qualitatively predicted experimental results at a given aggregate velocity. Error bars indicate the SEM of averaged experimental data from each group at each measured point. (D) Predicted versus experimental actin comets tails induced by aggregates with a similar number of Nck SH3 molecules (12,000–22,000 molecules). Experimental data were divided into five groups by velocity (n = 2–11). The mean experimentally measured actin concentrations from linescans were compared with Virtual Cell predictions. Virtual Cell simulations predicted experimental results at a given aggregate size. Error bars indicate the SEM of averaged experimental data from each group at each measured point. (E) Four representative comparisons chosen from 145 experimentally measured actin comet tails with corresponding simulations. The following parameters were used for simulations run with the experimentally measured size (Exp.) and velocity of individual Nck SH3 aggregates (VCell): 17,000 molecules, 0.04 μm/s (top left); 10,000 molecules, 0.050 μm/s (top right); 17,000 molecules, 0.057 μm/s (bottom left); and 17,000 molecules, 0.120 μm/s (bottom right).

overprediction of actin concentration downstream of the peak (this overprediction is most likely caused by the absence of actin-depolymerizing factors, such as cofilin or gelsolin, in our models). Thus, the Virtual Cell model predicts actin polymerization induced by an individual Nck SH3 aggregate. These data demonstrate that even though aggregate size and velocity are independent and cannot individually predict characteristics of actin polymerization, including both parameters in a biochemical model is predictive of actin polymerization downstream of Nck SH3 aggregates.

Actin polymerization is highly sensitive to Nck density

Although previous studies have demonstrated that high local Nck density results in localized actin polymerization (Scaplehorn et al., 2002; Rivera et al., 2004, 2006; Oser et al., 2010), the quantitative relationship between Nck density and actin polymerization has not been examined. We addressed this question directly using the aforementioned approach to quantify aggregate and comet tail characteristics in vivo. To produce aggregates containing different densities of Nck SH3 molecules, the fluorescent Nck fusion protein (CD16-7–mCherry–Nck SH3–HA) was co-expressed with a dummy fusion lacking Nck SH3 domains (CD16-7–mCerulean-HA) at a variety of ratios in NIH-3T3 fibroblasts stably expressing YFP-actin. Western blots were performed to ensure that varying the amount of each transfected construct resulted in the expected levels of expression of Nck SH3 and dummy fusion proteins (Fig. S1 C). In cotransfected fibroblasts, antibody-induced aggregation resulted in the formation of aggregates composed of both Nck SH3 and dummy molecules, as indicated by colocalized mCherry and mCerulean fluorescence; total amounts of each species were quantified for each aggregate.

Qualitative assessment of aggregates indicated that actin polymerization was highly sensitive to Nck density (Fig. 3 and Video 2). Aggregates composed of 0–20% Nck SH3 induced no detectable local actin polymerization (Fig. 3 A), whereas

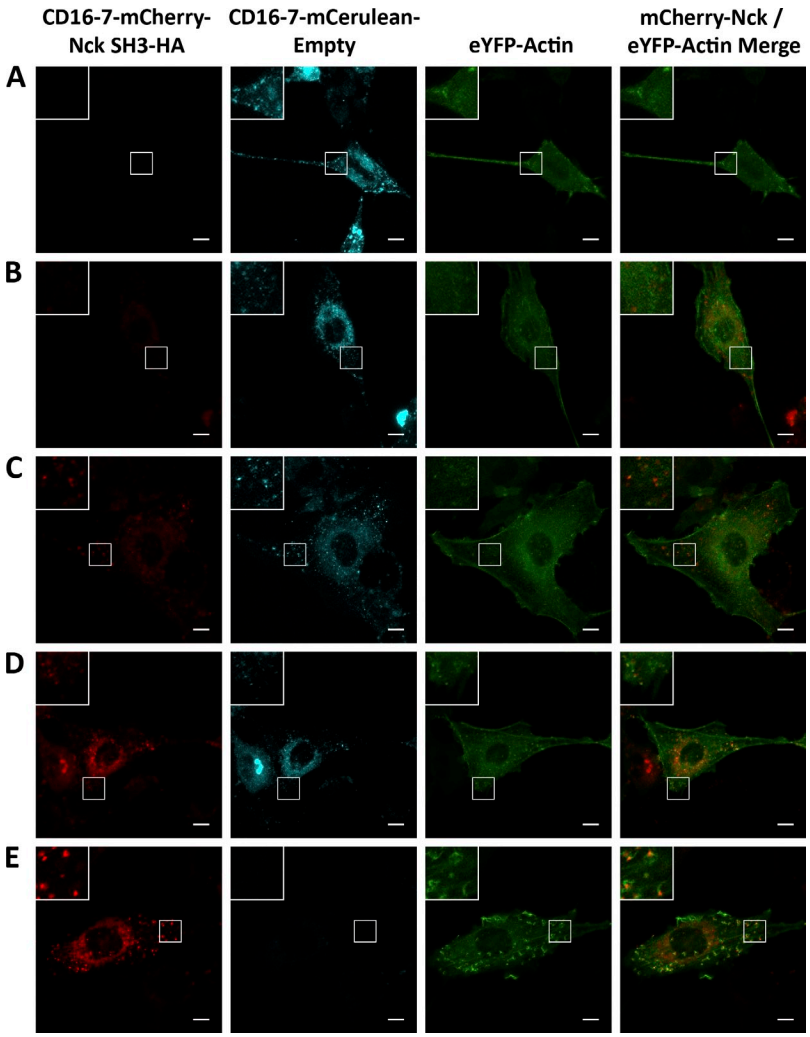

Figure 3. **Representative experimental images of aggregates containing different densities of Nck SH3 molecules.** (A–E) To test the effect of decreasing Nck SH3 density on localized actin polymerization, Nck SH3 domains with dummy fusion proteins were cotransfected and aggregated, resulting in aggregates of varying density. In individual images, CD16-7–mCherry–Nck SH3–HA is red, CD16-7–mCerulean-HA is cyan, and YFP-actin is green. For the mCherry-Nck/YFP-actin merged images, brightness and contrast have been adjusted to allow for comparison of Nck SH3 density-dependent actin polymerization associated with Nck SH3 aggregates. Higher magnifications of clusters are shown in the insets. Bars, 10 µm. (A) Aggregates containing 80–100% dummy and 0–20% Nck SH3 (0–5,000 Nck SH3/µm^2) induce no detectable actin polymerization. (B) Aggregates containing 60–80% dummy and 20–40% Nck SH3 (5,000–10,000 Nck SH3/µm^2) induce minimal actin polymerization that results in the formation of sparse actin spots. (C) Aggregates containing 40–60% dummy and 40–60% Nck SH3 (10,000–15,000 Nck SH3/µm^2) induce actin polymerization that results in the formation of dense actin spots. (D) Aggregates containing 20–40% dummy and 60–80% Nck SH3 (15,000–20,000 Nck SH3/µm^2) induce actin polymerization that results in the formation of dense actin spots or short actin comet tails. (E) Aggregates containing 0–20% dummy and 80–100% Nck SH3 (20,000–25,000 Nck SH3/µm^2) induce actin polymerization that results in the formation of a robust actin comet tail.

aggregates composed of 20–80% Nck SH3 induced actin polymerization ranging from light actin spots slightly above the background YFP-actin fluorescence to dense actin spots (Fig. 3, B–D). Aggregates composed of 80–100% Nck SH3 induced actin polymerization in the form of robust actin comet tails (Fig. 3 E).

These qualitative observations were supported by quantitative measurements of comet tail properties. Comet tail length, total number of actin molecules in the comet tail core, peak actin concentration, and distance between aggregate centroid and peak actin concentration were plotted against Nck SH3 density (Fig. 4). Peak actin concentration increased in a nonlinear fashion until it plateaued at 90% Nck SH3 density, whereas all other metrics of actin polymerization increased in a nonlinear fashion from 0 to 100% Nck SH3 density. Interestingly, aggregate velocity, which we previously showed to be independent of aggregate size (Fig. 1 C), has a strong dependency on Nck SH3 density (Fig. 4 A). With regard to the actin distributions in comet tails (Fig. 4, B–E), statistically significant differences were observed between the bins of Nck SH3 domain densities. Surprisingly, even the 80–99 and 100% densities displayed significant differences in comet tail length, number of comet tail F-actin subunits, and the distance between the Nck cluster and the peak actin in the comet (Fig. 4, B, C, and E). Thus, we conclude that the dependence of comet features on Nck SH3 domain density is highly nonlinear: small decreases in density <100% lead to disproportionately large decreases in actin polymerization. This strong density dependence prompted us to use our Virtual Cell model to evaluate different specific quantitative models of Nck SH3–dependent actin polymerization.

Alternative models of actin polymerization induced by the Nck–N-WASp–Arp2/3 pathway

Our original kinetic model for actin dendritic nucleation (Ditlev et al., 2009) was concerned with rates of actin polymerization at an activated lamellipodium and did not address the mechanism of Arp2/3 complex activation; we simply activated the Arp2/3 complex as it was recruited to the membrane. To understand the behavior shown in Fig. 4, however, it is necessary to explicitly consider the mechanisms for Nck recruitment of N-WASp and its activation of the Arp2/3 complex. In the simplest mechanism, one Nck molecule binds and activates a single N-WASp, which in turn binds and activates a single Arp2/3 complex in a 1:1:1 stoichiometry. We mathematically describe the 1:1:1 mechanism using mass-action kinetics for both N-WASp and Arp2/3 complex activation as follows: $k_f \times$ Nck SH3 $\times$ N-WASp $- k_r \times$ active

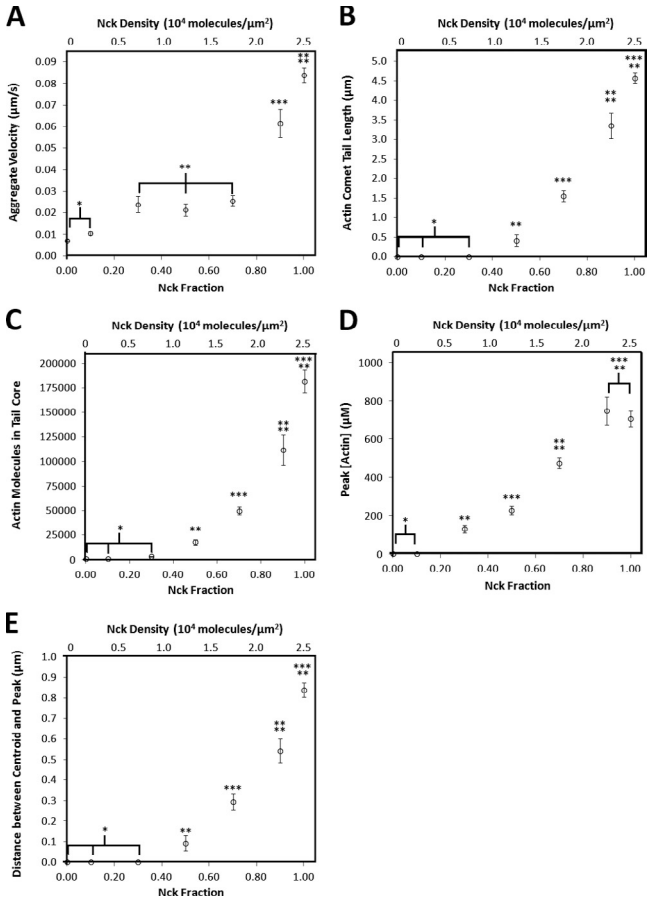

Figure 4. **Quantitative analysis of aggregates of various Nck SH3 density.** (A–E) Aggregates were divided into different groups based on their Nck SH3 density. Measured characteristics of individual aggregates were averaged and plotted against Nck SH3 density. Error bars indicate SEM of each density group. Significance is indicated by asterisks above data points ($P < 0.05$), with each notation indicating a significant difference between each set of data. The plots show that increasing Nck SH3 density results in a nonlinear increase in the velocity of aggregates (A), actin comet tail length (B), number of actin molecules in the comet tail core (C), the peak actin concentration in actin foci or comet tails (D), and the distance between the aggregate centroid and the peak actin concentration in aggregate-induced actin structures (E). These data are also presented as the experimental dataset in Fig. 5 to allow for comparison with model predictions.

N-WASp (for N-WASp activation) and $k_f \times$ active N-WASp $\times$ Arp2/3 $- k_r \times$ active Arp2/3 (for Arp2/3 activation).

However, evidence has suggested that two N-WASp molecules are required to recruit and activate a single Arp2/3 complex, thus requiring a stoichiometry of two Nck/two N-WASp/one Arp2/3 to induce actin polymerization (Higgs and Pollard, 2000; Padrick et al., 2008, 2011; Sallee et al., 2008; Padrick and Rosen, 2010; Ti et al., 2011). In this 2:2:1 reaction scheme, Nck SH3 activation of N-WASp is described as a bimolecular interaction, the same as that used in the 1:1:1 reaction scheme. Unlike the 1:1:1 reaction scheme, Arp2/3 complex activation is modified to account for its dependence on N-WASp dimerization. The tightly packed lattice of molecules generated by antibody-induced aggregation of CD16-7 molecules can be characterized by the mean number of N-WASp binding sites and the mean number of Arp2/3 complex binding sites per lattice site. We derive that the activation mechanism for the 2:2:1 scheme for N-WASp activation and Arp2/3 activation, respectively, is

$$k_f \times \text{Nck SH3} \times \text{N-WASp} - k_r \times \text{active N-WASp and}$$

$$\text{total lattice sites} \times \left(\frac{3}{2}\right) \times k_f \times \left(\frac{\text{active N-WASp}}{\text{total lattice sites}}\right)^2 \times \text{Arp2/3} - k_r \times \text{active Arp2/3},$$

where the factor of (3/2) represents the number of nearest neighbors that can participate in Arp2/3 complex binding while preventing overcounting. A detailed description of the derivation of the 2:2:1 reaction mechanism can be found under Modeling 2:2:1 and 4:2:1 Nck–N-WASp–Arp2/3 complex binding using Virtual Cell in Materials and methods.

To assess which mechanism was correct, the effect of Nck SH3 aggregate density on actin nucleation and polymerization was modeled using the aforementioned mechanisms of Nck SH3 activation of the N-WASp and Arp2/3 complex (1:1:1 and 2:2:1). Because there is a reported 180-fold–higher binding affinity for dimerized N-WASp VCA (verprolin, cofilin, and acidic) to Arp2/3 (2:2:1 model) versus monomeric N-WASp VCA to Arp2/3 (1:1:1 model; Padrick et al., 2008), the k_r was decreased by 180 fold (from 1.6 to 0.009 s^{-1}) to account for a decreased Arp2/3 complex off rate caused by stabilization of the multivalent complex. A 2D geometry of 1,400 mesh units (25.0 μm × 14.0 μm, 100 × 14 mesh elements) was created and used to test actin polymerization after Arp2/3 activation. Simulations were performed with five aggregate sizes (corresponding to 1,560, 6,250, 14,000, 25,000, and 39,000 molecules when extrapolated to three dimensions), seven densities of Nck SH3 domains (0, 10, 30, 50, 70, 90, and 100% Nck), and seven velocities (0, 0.005, 0.010, 0.025, 0.050, 0.100, and 0.150 μm/s). These parameters were selected to span the range of experimentally measured values. This amounted to 490 simulations, 245 for each of the two postulated stoichiometries. Once steady state was reached, actin comet tail length, total number of actin molecules in the comet tail core, peak actin concentration, and distance from aggregate centroid to the peak actin concentration were calculated from each simulation.

Comparison of simulation results and experimental results revealed striking differences in actin polymerization patterns, depending on the density of Nck SH3 (Fig. 5, A–D). The experimental data at a given density is a mean over patches with varying sizes and velocities. To properly compare our simulation results with these data, for each density, we ran several simulations with varying patch sizes and velocities and then took a weighted mean of these results to reflect the actual experimental population. This averaging procedure produced a nonmonotonic, jagged-looking curve for the 1:1:1 mechanism. Furthermore, actin polymerization increased in an approximately linear fashion as the density of Nck increased from 0 to 50%, predicting that actin polymerization would be experimentally measureable even when induced by the lowest measured densities of Nck SH3 aggregates. When the 2:2:1 mechanism was used to induce actin polymerization, actin polymerization increased in an approximately linear fashion from 30 to 90% Nck density with a nonlinear increase at

100% Nck density. When compared with experimental data, results from the 2:2:1 model, although much improved over the 1:1:1 stoichiometry, overpredicted the amount of actin polymerization induced by aggregates composed of 30–90% Nck.

The poor fit between model predictions and experimental data prompted us to explore other possible Arp2/3 complex activation mechanisms. One possible mechanism involves endogenous Nck being recruited to aggregates, for example through binding to other sites on the proline-rich region of N-WASp or proteins to which the Nck SH2 domain or SH3 domains can bind, resulting in a nonmeasured increase in Nck SH3 domains at the aggregates. In this scenario, recruitment of endogenous Nck could then lead to an increase in the number of N-WASp molecules bound, resulting in the nonlinear actin polymerization observed in our experimentally measured data. To determine the potential for this mechanism to cause the observed nonlinear actin polymerization downstream of Nck SH3 aggregates, we first compared the amount of expressed mCherry–Nck SH3 to endogenous Nck in lysates obtained from transfected NIH-3T3 cells by Western blotting (Fig. S1 D). The Western blot results, when normalized for transfection efficiency, indicate that mCherry-Nck exists at an approximately sevenfold-higher concentration than endogenous Nck before aggregation in transfected cells. After aggregation, the local concentration of mCherry-Nck fusions would be even greater, leading us to conclude that although endogenous Nck may be present at aggregates of Nck SH3 domains, its effect on nonlinear actin polymerization would be minimal.

Another possible mechanism involves WASp-interacting protein (WIP), a protein known to bind independently to the middle SH3 domain of Nck and to the WH1 domain of N-WASp (Antón et al., 1998; Benesch et al., 2002; Tehrani et al., 2007; Weisswange et al., 2009). WIP has been shown to be present at Nck SH3 aggregates by immunofluorescence (Rivera et al., 2004). Other studies have shown that WIP is essential for optimal actin polymerization downstream of Nck and N-WASp (Antón et al., 1998; Frischknecht et al., 1999; Moreau et al., 2000; Benesch et al., 2002; Sasahara et al., 2002; Tehrani et al., 2007). We postulated that while one Nck molecule binds directly to the proline-rich domain of N-WASp, a second Nck molecule might bind the WH1 domain of N-WASP indirectly, bridged by WIP (Padrick and Rosen, 2010). In this model, each activated N-WASp is bound to one WIP and two Nck molecules. Because two active N-WASp molecules are required for efficient Arp2/3 complex activation, our proposed Nck/N-WASp/Arp2/3 stoichiometry is 4:2:1. The approach used to mathematically describe this mechanism involves weight and probability-dependent N-WASp and Arp2/3 complex activation and is as follows for N-WASp and Arp2/3 activation, respectively:

$$\text{total lattice sites} \times \left(\frac{3}{2}\right) \times k_f \times \text{N-WASp} \times \left(\frac{\text{Nck SH3}}{\text{total lattice sites}}\right)^2 \times \left(\frac{1}{1-3\left(\frac{\text{active Arp}}{\text{total lattice sites}}\right)-\left(\frac{\text{active N-WASp}}{\text{total lattice sites}}\right)}\right) - k_r \times \text{active N-WASp and}$$

$$\text{total lattice sites} \times \left(\frac{3}{4}\right) \times k_f \times \text{Arp2/3} \times \left(\frac{2 \times \text{active N-WASp}}{\text{total lattice sites}}\right)^2 \times \left(\frac{1}{1-3\left(\frac{\text{active Arp}}{\text{total lattice sites}}\right)-\left(\frac{\text{active N-WASp}}{\text{total lattice sites}}\right)}\right) - k_r \times \text{active Arp2/3.}$$

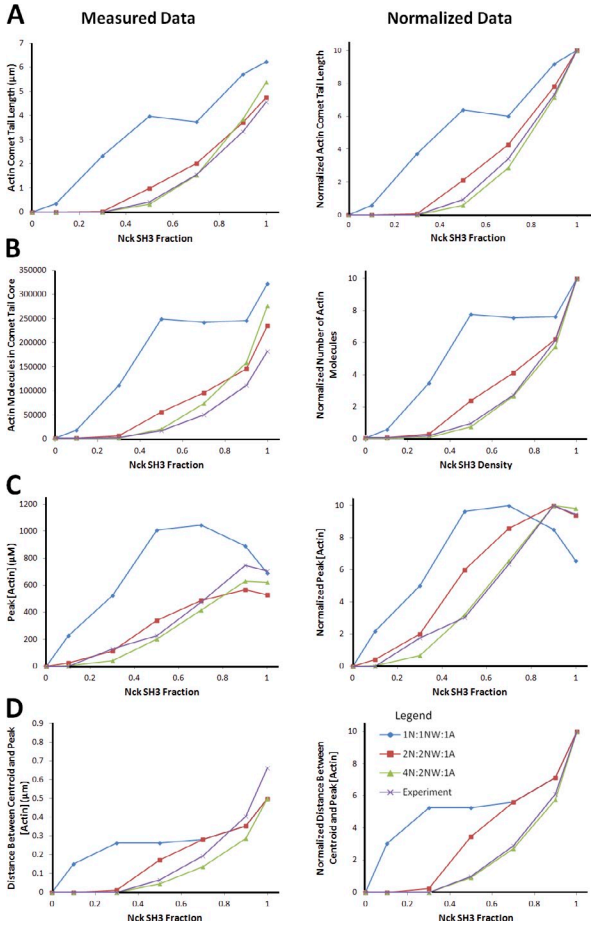

Figure 5. **Comparison between experimental results and Virtual Cell biochemical model predictions from simulations using different mechanisms of Arp2/3 activation.** (A–D) Quantitative Virtual Cell biochemical simulations were performed using three different mechanisms of N-WASp (NW) and Arp2/3 complex activation, five different aggregate sizes, six different aggregate velocities, and seven different Nck SH3 densities. Models were simulated using experimentally measured aggregate sizes, velocities, and densities. Simulation results were weighted based on experimentally measured aggregate size and velocity distributions to allow for an accurate comparison of predicted and experimental results. The plots show comparisons of simulation results from models using one Nck/one N-WASp/one Arp2/3, two Nck/two N-WASp/one Arp2/3, or four Nck/two N-WASp/one Arp2/3 with experimentally measured actin comet tail length (A), number of actin molecules in the comet tail core (B), peak actin concentration (C), and distance between aggregate centroid and peak actin concentration (D). For each measured actin comet tail characteristic, the 4:2:1 Nck/N-WASp/Arp2/3 activation scheme best predicted experimental results, suggesting that this mechanism, and not the 1:1:1 or 2:2:1 mechanism, was responsible for the activation of Arp2/3 downstream of Nck SH3 domains. For graphs on right, data have been normalized to the maximum values within each group to allow for another comparison of predicted and experimental results. The data for the experimental datasets are duplicated from Fig. 4 for comparison with model predictions.

Here, the factors of (3/2) and (3/4) represent the number of nearest neighbors that can participate in N-WASp or Arp2/3 complex binding while preventing overcounting (see Materials and methods for details on how these formulae were derived).

Using this 4:2:1 stoichiometry, we found a remarkable correspondence between experimentally measured comet tail values and computationally predicted values. Quantitative predictions of comet tail length and the total number of actin molecules in the comet tail core were virtually identical to the measured data from 0 to 70% and slightly overpredicted at 90 and 100%, which was expected, given our previous simulations in Fig. 2 E showing a consistent overprediction of actin, likely caused by the absence of actin-depolymerizing factors in our model (left graphs in Fig. 5 [A and B]). Predicted peak actin concentration and distance between aggregate centroid and peak actin concentration were not identical to experimentally measured values, but the curves were very similar (i.e., the model accurately predicted the ratios of values between different density groups; left graphs in Fig. 5 [C and D]). Furthermore, when predicted and experimentally measured data were internally normalized to the maximum value within each group, as shown in the right graphs of Fig. 5 (A–D), experimental data curves were virtually identical to simulation results from models run with the 4:2:1 mechanism. These results strongly suggest that of the three models tested, the 4:2:1 model most accurately predicts the effects of Nck density on experimentally measured actin comet tail properties. It is also important to note that the differences between the 1:1:1 model used in Fig. 2 and the more accurate 4:2:1 model are insignificant (≤10% for all measurements) when Nck SH3 density is at 100%, allowing us to use the 1:1:1 model predictions for results shown in Fig. 2.

WIP is essential for activation of the Arp2/3 complex by Nck aggregation

To test our hypothesis that WIP functions as a bridge between Nck and N-WASp in Nck-induced actin polymerization (Antón et al., 1998, 2002; Tehrani et al., 2007; Weisswange et al., 2009), Nck SH3 domains were aggregated in WIP wild-type (WT) and knockout (KO) mouse embryonic fibroblasts (MEFs). As expected, Nck aggregates induced actin comet tail formation in WIP WT cells (Fig. 6 A [top] and Video 3). In contrast, Nck aggregates did not induce actin comet tails in WIP KO cells (Fig. 6 A [bottom] and Video 3). To confirm that WIP is necessary for Nck-induced actin comet tail formation, WIP KO MEFs were rescued with GFP-WIP. Nck aggregates induced actin comet tails with GFP-WIP localizing to the Nck aggregate at the front of the actin comet tail (Fig. 6 B and Video 3). The role of WIP was further examined by testing N-WASp recruitment to Nck aggregates in WIP KO and WT MEFs and WIP recruitment to Nck aggregates in N-WASp KO and WT MEFs. In WIP KO MEFs, GFP–N-WASp was not recruited to Nck aggregates, nor was actin polymerization induced by Nck aggregates (Fig. 6 C [top]). Conversely, GFP–N-WASp is recruited to Nck aggregates in WIP WT MEFs, and actin polymerization is induced (Fig. 6 C [bottom]). In both N-WASp KO and WT MEFs, GFP-WIP is recruited to Nck SH3 aggregates. As expected, actin polymerization is only induced in N-WASp WT cells (Fig. 6 D; Rivera et al., 2004). These data confirm the suggestion by Weisswange et al. (2009) that WIP is required for recruitment of N-WASp to Nck.

Having established that WIP is essential for N-WASp recruitment to Nck SH3 aggregates, we then tested whether WIP may function as a bridge between one Nck molecule and N-WASp, allowing a second Nck molecule to bind and activate N-WASp by binding its proline-rich domain. We hypothesized that because WIP binds exclusively to the middle SH3 domain of Nck (Antón et al., 1998), N-WASp would be recruited, through WIP, to aggregates composed of Nck SH3 domain 2, whereas aggregates composed of both Nck SH3 (2) and Nck SH3 (1+2+3) would induce actin structures similar to those seen induced by 100% Nck SH3 (1+2+3) aggregates. To test these hypotheses, CD16-7 fusion proteins containing Nck SH3 (1), Nck SH3 (2), Nck SH3 (1+2+3), and/or the CD16-7–dummy fusion were aggregated and visualized using Alexa Fluor 647–labeled secondary antibody. The results of these coaggregation experiments are illustrated in Fig. S3. As previously shown (Fig. 3), 50 and 100% Nck SH3 (1+2+3) aggregates recruited GFP–N-WASp and induced actin polymerization in the form of actin spots and actin comet tails, respectively. Aggregation of Nck SH3 (1), which does not strongly bind either WIP or N-WASp, did not recruit GFP–N-WASp nor induce actin polymerization. In contrast, GFP–N-WASp was recruited to Nck SH3 (2) aggregates, and these aggregates induced the formation of sparse actin spots but not comet tails. Aggregates composed of 50% Nck SH3 (2) and 50% Nck SH3 (1+2+3), however, recruited GFP–N-WASp and induced the formation of robust actin structures similar to those induced by 100% Nck SH3 1+2+3 aggregates. These observations suggest that N-WASp is fully activated only when binding sites for both WIP (Nck SH3 2) and N-WASp (Nck SH3 1+2+3) are present in aggregates.

These results demonstrate that WIP plays an essential role in Nck-induced actin polymerization through the N-WASp–Arp2/3 pathway by recruiting N-WASp to Nck. Furthermore, they lend experimental support to our modeling-based prediction that a single Arp2/3 complex is activated downstream of four Nck molecules and two N-WASp molecules (with WIP providing the bridge between one Nck molecule and the WH1 domain of N-WASp).

Discussion

Using a combination of computational modeling and quantitative experimentation, we have uncovered two novel attributes of Nck-stimulated actin polymerization in living cells: (1) its strong dependence on the local density rather than the absolute number of Nck molecules and (2) the apparent requirement of a 4:2:1 Nck/N-WASp/Arp2/3 stoichiometry for the assembly of a productive complex (model summarized in Fig. 7). In addition, the present studies underscore the power of combining computational predictions with rigorous hypothesis testing using quantitative experimental approaches. The computational model that best fit in vivo experimental evidence was one in which four Nck molecules in close physical proximity were

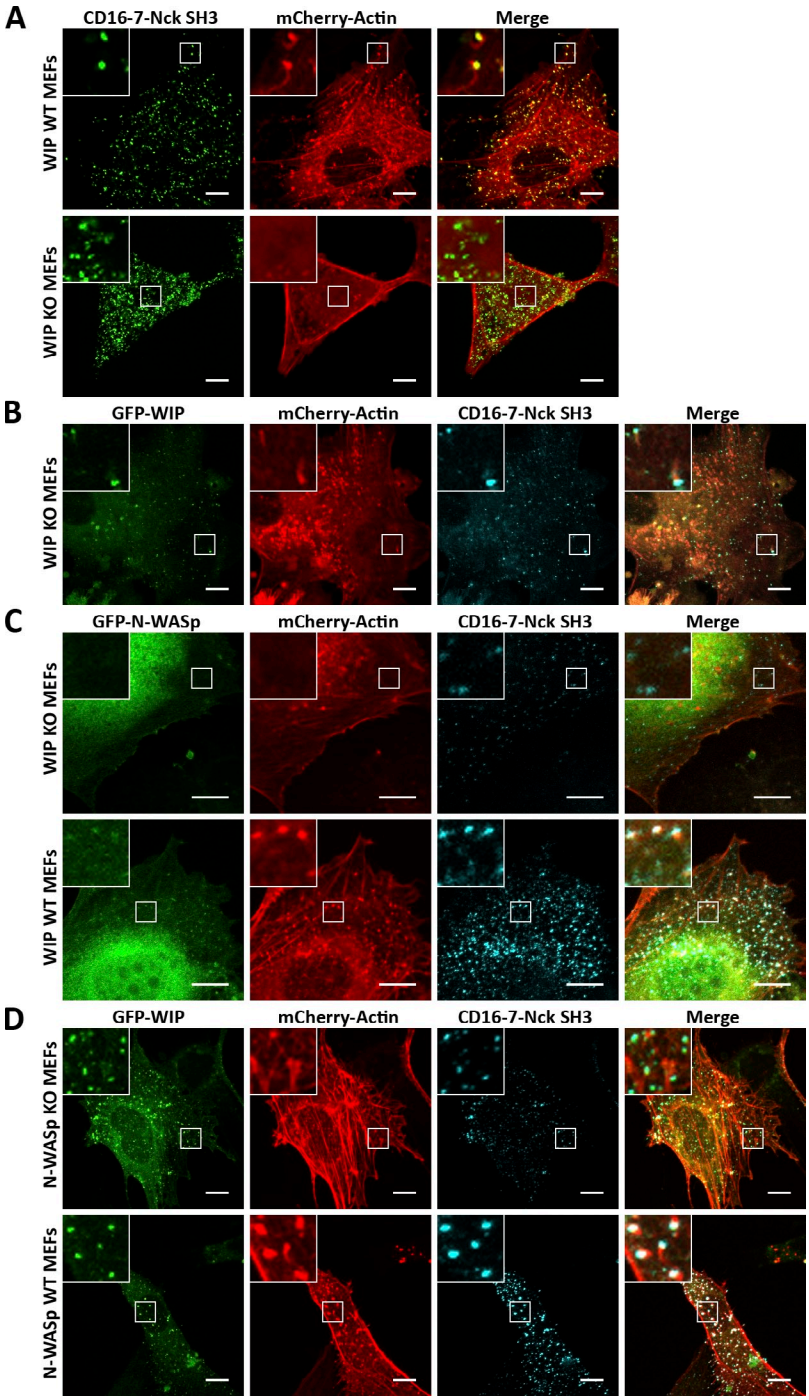

Figure 6. **WIP is an essential component of the Nck–N-WASp–Arp2/3 pathway.** (A–D) Confocal images of either WIP WT and KO or N-WASp WT and KO MEFs transfected with a combination of mCherry-actin, membrane-bound Nck SH3 fusion, and GFP-WIP or GFP–N-WASp demonstrate the necessity of WIP for Nck-induced, N-WASp–dependent actin polymerization. Higher magnifications of clusters are shown in the insets. Bars, 10 µm. (A) Antibody-induced aggregation of Nck SH3 domains (green) induces the formation of actin comet tails (red) in WIP WT MEFs (top) but does not induce actin polymerization in WIP KO MEFs (bottom). (B) Aggregation of Nck SH3 domains (cyan) in WIP KO MEFs rescued with GFP-WIP (green) induces actin comet tails (red) similar to those seen in WIP WT MEFs. (C) Nck SH3 aggregates (cyan) neither recruit GFP–N-WASp (green) nor induce actin polymerization (red) in WIP KO MEFs (top), whereas Nck SH3 aggregates in WIP WT MEFs both recruit GFP–N-WASp and induce actin polymerization (bottom). (D) Nck SH3 aggregates (cyan) recruit GFP-WIP (green) in both N-WASp KO MEFs (top) and N-WASp WT MEFs (bottom) but only induce actin polymerization (red) in N-WASp WT MEFs.

required to activate an Arp2/3 complex to nucleate new actin filaments. The scaffolding protein WIP provided a plausible mechanism for engaging two Nck molecules to bind and activate a single N-WASp molecule, and further experimentation demonstrated a requirement for WIP for Nck-induced actin polymerization. Accordingly, we propose that one Nck molecule directly binds (via all three SH3 domains) the proline-rich region of N-WASp, whereas another Nck molecule indirectly contributes to the formation of an active N-WASp complex through an interaction (via the second Nck SH3 domain) with WIP. The 4:2:1 Nck/N-WASp/Arp2/3 stoichiometry in our working model is also consistent with the requirement for dimerization/oligomerization for the enhancement of N-WASp activity by SH3 domain–containing proteins first demonstrated by Padrick et al. (2008).

The cooperative interaction of Nck and WIP in N-WASP activation in vivo demonstrated in this study is further supported by previous findings of colocalization of Nck and WIP at sites of actin polymerization in cells and from in vitro studies of actin polymerization using purified components. Tehrani et al. (2007) demonstrated that N-WASp activity increased when both Nck and WIP were present in reaction mixtures compared with N-WASp activity when only Nck or WIP was included. In addition to these in vitro results, Weisswange et al. (2009)

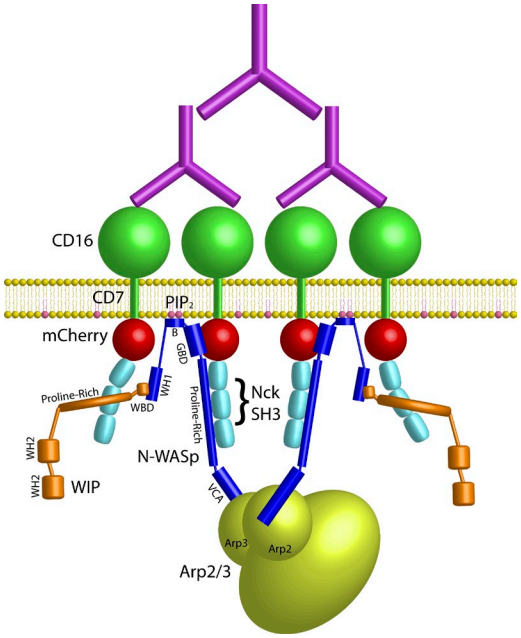

Figure 7. **Proposed 4:2:1 Nck/N-WASp/Arp2/3 mechanism leading to actin polymerization.** In our proposed mechanism, two Nck molecules bind each N-WASp; one Nck molecule binds directly to the proline-rich region of N-WASp, whereas a second Nck molecule binds the proline-rich region of WIP, which in turn binds the WH1 domain of N-WASp. Two activated N-WASp molecules then bind and activate Arp2/3, resulting in actin filament nucleation and polymerization. Although not drawn precisely to scale, the molecular mechanism presented here is intended to demonstrate the spatial arrangement of all proteins near the membrane in our experimental system. B, basic region; GBD, GTPase binding domain; WBD, WASp binding domain.

suggested that WIP is required for N-WASp recruitment to Nck during Vaccinia virus infection in vivo.

The mechanistic insights from the current study provide a new conceptual framework for understanding critical cellular processes that rely on Nck-stimulated F-actin assembly. For instance, during both invadopodia formation in tumor cells and T cell activation, processes that involve N-WASp and WASp, respectively, scaffolding proteins are phosphorylated at multiple tyrosine residues and thereby recruit multiple Nck molecules. In T cell activation, SLP-76 is phosphorylated at three sites, which can recruit Nck, and the Nck/SLP-76 ratio at sites of T cell receptor activation is 2:1 (Barda-Saad et al., 2010). If any combination of these sites is mutated, actin polymerization is impaired during T cell activation. Similarly, during invadopodia formation, cortactin is phosphorylated at two tyrosine residues, each of which can recruit Nck. If either phosphotyrosine site is mutated, actin polymerization is ablated, and no invadopodia form (Oser et al., 2010). Furthermore, WIP is present at sites of both T cell activation and invadopodia formation (Sasahara et al., 2002; Yamaguchi et al., 2005). Additionally, mutations in WASp-affecting WIP binding are found in ∼50% of patients with Wiskott–Aldrich syndrome, an immunodeficiency disorder in which lymphocytes, including T cells, cannot properly activate or migrate as a result of actin cytoskeletal abnormalities (Stewart et al., 1999; Rong and Vihinen, 2000; Rajmohan et al., 2009). Such mutations would prevent WIP from binding and recruiting WASp to Nck at sites of T cell receptor activation, decreasing localized actin polymerization. Thus, our proposed mechanism underscores the importance of the cooperative interactions of WIP and Nck in WASp or N-WASp activation, leading to actin polymerization in physiological systems.

Another study has demonstrated the importance of effector molecule density on N-WASp activation. In their study, Papayannopoulos et al. (2005) showed that as the density of PIP_2 (which binds N-WASp and promotes its activation) on the membrane increased, actin polymerization downstream of N-WASp increased in a nonlinear manner, similar to what we observed for Nck. Our results, coupled with their data, suggest such cooperative interactions are general mechanisms that prevent adventitious activation by low levels of input signal. For instance, a strong external stimulus that activates many receptors on a small region of membrane will greatly increase the density of phosphotyrosine residues in the stimulated region of the membrane. These phosphotyrosine residues will recruit Nck, resulting in locally high Nck density, which in turn will induce a strong actin response to the stimulus. Conversely, if a weak external stimulus activates only a few receptors across the surface of a cell, the low density of phosphotyrosine residues will result in the recruitment of relatively few Nck molecules. The likelihood that four Nck molecules will be recruited immediately adjacent to each other will be extremely low. Because four Nck molecules are required to drive Arp2/3 activation, the cell will not mount a strong actin response to the stimulus. Thus, the 4:2:1 stoichiometry imposes a threshold below which there is little, if any, response. The requirement for four closely apposed Nck molecules will also favor responses to proteins with multiple tyrosine phosphorylation sites or instances in which tyrosine kinases and their substrates are clustered to promote high local density of phosphorylated sites.

In summary, using computational modeling and experimental manipulation of Nck SH3 domains, we provide functional insights into the quantitative relationship between Nck and downstream actin polymerization as well as describe a previously unappreciated mechanism by which Nck induces N-WASp–dependent actin polymerization. The 4:2:1 Nck/N-WASp/Arp2/3 mechanism described by our study may also provide insights into the molecular basis for T cell activation and invadopodia formation in invasive cancers. In addition to unraveling the complex molecular interactions driving Nck- and N-WASp–dependent actin polymerization, our quantitative biochemical modeling and precise quantitative experimental techniques are likely to be useful in further studying Nck as well as other cytoskeletal effectors.

Materials and methods

Biochemical modeling

All simulations were performed with the Virtual Cell modeling software, using a simplified actin dendritic nucleation model based on the actin dendritic nucleation model published in Ditlev et al. (2009). The original model consists of 46 chemical species and 106 reactions and provides an accurate description of both in vitro and in vivo actin networks. However, the original model runs slowly when used with realistic spatial geometries, and we therefore simplified this original model to decrease computation time. We used four approaches to simplify the model: eliminate unnecessary species, eliminate unimportant reactions, lump two species into a

single species when appropriate, and use computationally faster functions wherever possible (Tables S2–S4). The final simplified model consists of 26 species and 67 reactions and generally runs 3–30 times faster than the old model, depending on simulation parameters and geometry. To verify that the simplified model sufficiently described actin polymerization, simulations were run using both the simplified and original models. Results from each model agreed to within 10%. The consistency between results from the simplified model and the original model allowed us to use the simplified model for our study. The models used in this study can be found in the Online supplemental material section as well as in the Virtual Cell public database under user JDitlev with the following model names: Nck Induces Actin Comet Tail Formation Single NWASP Activation of Arp2/3 Simplified Actin Dendritic Nucleation (1:1:1 model); Nck Induces Actin Comet Tail Formation Dimer NWASP Activation of Arp2/3 Simplified Actin Dendritic Nucleation (2:2:1 model); and Nck Induces Actin Comet Tail Formation Dimer Nck Binds NWASP With Dimer NWASP Activation of Arp2/3 Simplified Actin Dendritic Nucleation (4:2:1 model).

Viral production and infection

HEK293T cells were transfected by calcium phosphate precipitation with a pMSCV-puro retroviral vector containing YFP-actin plus viral packaging plasmids pMD.env and pMD.gag.pol. Medium containing virus was harvested within 48 h after transfection. NIH-3T3 fibroblasts were infected with YFP-actin–encoding virus in the presence of 2 µg/ml polybrene (Millipore). Infected cells were drug selected with 1.0 µg/ml puromycin (Sigma-Aldrich) for 4 wk to establish a stable cell line. Cells were kept for 5 wk for further experiments.

Plasmid construction, cell culture, transfection, immunoblotting, and antibody-induced Nck SH3 domain aggregation

Constructs encoding fusion proteins consisting of the extracellular domain of human CD16, the transmembrane domain of human CD7, mCherry, all three SH3 domains of human Nck, and an HA epitope tag were generated. Constructs encoding fusion proteins consisting of CD16, CD7, mCerulean, and HA tag (dummy) were also generated (Fig. S1 B). Expression of constructs was tested after NIH-3T3 fibroblast transfection using Western blotting. To test levels of CD16-7–mCherry–Nck SH3–HA versus CD16-7–mCerulean-HA (dummy) after transfections of different ratios of construct (CD16-Nck/CD16-dummy at 1:1 and 1:3), lysates from CD16-7–mCherry–Nck SH3–HA and CD16-7–mCerulean-HA cotransfected were obtained and subjected to SDS-PAGE. After transfer to nitrocellulose membrane, blots were probed with polyclonal anti-HA antibody (Santa Cruz Biotechnology, Inc.) to assess the expressed ratios of CD16-Nck/CD16-dummy proteins (Fig. S1 C). To test expression levels of CD16-7–mCherry–Nck SH3–HA compared with endogenous Nck, lysates from CD16-7–mCherry–Nck SH3–HA-transfected cells were obtained and subjected to SDS-PAGE. After transfer to nitrocellulose membrane, blots were probed with polyclonal anti-Nck affinity-purified antiserum to assess CD16-7–mCherry–Nck SH3–HA expression versus endogenous Nck expression (Fig. S1 D).

For imaging, stable YFP-actin–expressing NIH-3T3 cells were cultured in DME supplemented with 10% calf serum and 1% Pen/strep solution (Mediatech Inc.). Stable YFP-actin–expressing NIH-3T3 cells were cotransfected with vectors harboring mCherry-labeled Nck SH3 fusion and mCerulean-labeled dummy fusion constructs. After transfection, cells were passed to 35-mm glass-bottomed culture dishes (MatTek Corporation). Approximately 36 h after transfection, aggregation of membrane-bound Nck and/or membrane-bound mCerulean was accomplished through antibody-mediated cross-linking (Fig. S1 A). Cells were incubated with a monoclonal antibody against human CD16 (Santa Cruz Biotechnology, Inc.) at a concentration of 0.75 µg/ml in complete medium for 20 min at 37°C. After washing cells with complete medium to remove excess anti-CD16 antibody, cells were incubated with an unlabeled goat anti–mouse IgG (Thermo Fisher Scientific) at a concentration of 0.50 µg/ml for 30 min at 37°C. Unbound antibody was removed from the cells by washing with complete medium, and cells were immediately imaged using confocal microscopy.

Live-cell imaging and image analysis of Nck aggregates

For experiments shown in Figs. 1 and 2, NIH-3T3 fibroblasts were cotransfected with GFP-actin and mCherry-labeled Nck SH3 domain constructs. For experiments examining the effect of Nck SH3 density on actin polymerization (Figs. 3, 4, and 5), NIH-3T3 fibroblasts stably expressing YFP-actin were cotransfected with CD16/7-mCherry–Nck SH3–HA and/or CD16/7-mCerulean-HA constructs. Transfected cells were cultured in pH indicator–free DME (Invitrogen) in glass-bottomed culture dishes and maintained at 37°C using a stage/objective heating system (Carl Zeiss and Bioptechs, respectively). Live-cell images were obtained using a spinning microlens confocal system (UltraView; PerkinElmer) mounted on an inverted microscope (TE2000; Nikon) equipped with a charge-coupled device camera (Orca-ER Firewire; Hamamatsu Photonics) and a 40× 1.25 NA or 60× 1.4 NA oil immersion objective or a confocal microscope (LSM 780; Carl Zeiss) with a 63× 1.4 NA oil immersion objective using either MetaMorph (Molecular Devices) or ZEN (Carl Zeiss) software, respectively, to acquire the time-lapse images. This experimental procedure results in CD16 fusion protein aggregation on the membrane of cells; however, some of these aggregates may be internalized. Because of the thickness of NIH-3T3 fibroblasts and the z resolution of the confocal microscopes used in this study, it is difficult to determine which aggregates, if any, are internalized by the cell.

Using a previously described plug-in in ImageJ (National Institutes of Health), aggregates and actin comet tails were identified for further analysis in a nonbiased manner (Sallee et al., 2008). The algorithm relied on two user inputs for proper detection of mCherry–Nck SH3 aggregates: aggregate radius in pixels and intensity threshold. By defining a radius (i.e., 3–8 pixels) and minimum threshold (i.e., top 5% of intense pixels), most of the background fluorescence was eliminated, allowing for analysis of only specific aggregates that fit user-defined criteria. Detection of GFP-actin comet tails was accomplished using the same technique. After detection of both aggregates and comet tails, the software used a multipass algorithm to pair detected aggregates with comet tails for further analysis.

After aggregate and comet tail identification, MetaMorph was used to measure the fluorescent intensity of aggregates and comet tails, to measure length of comet tails, and to track comet tail polymerization over the course of the image time series. Algorithm-identified aggregates were analyzed for number of molecules (size) and velocity using the methods described in the next section. Corresponding comet tails, as identified by our algorithm, were analyzed for actin comet tail length, total fluorescent intensity, peak actin fluorescent intensity, and actin fluorescent distribution along the length of the tail.

Fluorescent protein quantification and fluorescence per molecule calculations

Two methods were used to determine the fluorescence per molecule of the mCherry-labeled Nck construct. These methods were both used in obtained data used in Figs. 1 and 2, whereas only the first method described here was used to obtain data used in Figs. 4 and 5. The first method used imaging a purified GST-tagged mCerulean or GST-tagged fusion protein containing all three Nck SH3 domains labeled with mCherry (Fink et al., 1998). A 10-µl droplet of purified fusion protein was placed in mineral oil and allowed to settle on the bottom of a glass-bottomed plate. Images from the center of the droplet were obtained using the spinning microlens confocal system previously described and analyzed for absolute fluorescence using MetaMorph and ImageJ analysis software. The maximum measured intensity of purified mCherry and mCerulean was 119 and 102 arbitrary units (AU; maximum of 255 AU), respectively. These intensities were higher than the maximum intensity measured from mCherry- or mCerulean-labeled aggregates (89 and 43 AU [maximum of 255], respectively), which ensured that extrapolation of aggregate intensity to unmeasured purified protein intensities was unnecessary, thus allowing for confident fluorescence per molecule calculations. The concentration of purified GST-mCherry-Nck fusion or GST-mCerulean proteins was calculated from A_{280} measurements obtained using a Nanodrop spectrophotometer (Thermo Fisher Scientific). The fluorescence per molecule was calculated using the fluorescence and concentration measurements of the GST-mCherry–Nck SH3 or GST-mCerulean–purified proteins.

The second method used imaging of transfected cells coupled with quantitative Western blotting (Wu and Pollard, 2005). Cells transfected with mCherry-labeled, membrane-bound Nck were evenly split 1:4 to four plates and allowed to grow overnight. For this method of fluorescence per molecule calibration, one plate was used to count the number of cells (both transfected and nontransfected) to determine the number of cells/plate and the transfection efficiency, one plate was used to obtain cell lysates, one plate was used to image total cell fluorescence from mCherry-Nck–transfected cells, and the final plate was used to image actin comet tails. Cell counts were obtained using a hemocytometer, and transfection efficiency was determined by counting both fluorescent and nonfluorescent cells using a brightfield microscope with a fluorescent filter for mCherry. Cell lysates were harvested from transfected cells, and the volume was measured. Lysates and GST-Nck-HA fusion proteins of known concentrations were subjected to SDS-PAGE, with GST-Nck-HA fusion proteins used to create a standard concentration curve used to determine the concentration of CD16-7–mCherry-Nck fusion proteins in transfected cells. After transfer to nitrocellulose membranes,

blots were probed with a polyclonal anti-HA antibody followed by goat anti–rabbit HRP-conjugated secondary antibody. Blots were developed, and band density was measured using tools available in ImageJ analysis software. Using the GST-Nck-HA standard curve, lysate concentration of mCherry-labeled Nck fusion protein was determined. Using the total number of cells and transfection efficiency, as determined through cell counting, the measured lysate volume, and the concentration of CD16-7–mCherry-Nck measured by Western blotting, the total number of CD16-7–mCherry–Nck SH3 molecules was calculated. Images of transfected and nontransfected cells were obtained using the spinning microlens confocal system previously described and analyzed for total cell fluorescence using MetaMorph analysis software (images were also used to confirm the transfection efficiency of each experiment by counting the number of transfected cells vs. nontransfected cells). The total integrated fluorescence density of transfected cells was measured using MetaMorph. Using the calculated number of mCherry-Nck per fluorescent cell and the measured integrated density of fluorescent cells, the fluorescence per molecule was calculated.

The calculated fluorescence per molecule from each method was compared and found to be within 2% of each other for each experimental run, as both calibrations were performed for each experimental run used to collect data used in Figs. 1 and 2. As previously stated, because of the similarity between the methods, only the first described method was used for all density experiments described in Figs. 4 and 5. To obtain the fluorescence per molecule of individual aggregates, each aggregate was convolved using the point spread function. The integrated density of each convolved aggregate was then divided by the calculated total fluorescence per molecule to obtain the number of fluorescently tagged molecules per aggregate.

Because mCherry-Nck aggregates were quantified using confocal fluorescent microscopy, it was necessary to determine whether aggregation of fluorescent mCherry–Nck SH3 was inducing autoquenching of the mCherry, a phenomenon previously observed in other fluorophores at high concentrations (Bunting et al., 1989; Duchen and Biscoe, 1992). NIH-3T3 fibroblasts were transfected with CD16-7–mCherry–Nck SH3. After transfection, cells were split at 1:2 to one glass-bottomed dish for imaging and one culture dish for lysate collection. Before imaging, lysates were collected from the split transfected cells. Western blots were performed and quantified, as previously described. 88 transfected control cells, in which aggregation was not induced, and 35 experimental cells, in which aggregation was induced, were imaged using the previously described spinning-disc microscope. Total cellular fluorescence was measured using MetaMorph in both control and experimental cells. Using our previously described method of fluorescence per molecule calculations by fluorescence imaging and Western blot analysis, it was determined that the concentration of mCherry in aggregates was not inducing autoquenching of the fluorophore, as control and experimental measurements resulted in 96% similar fluorescence per molecule calculations. These results are described in Table S1.

To analyze GFP- and YFP-actin, a cellular concentration of 200 µM actin (both native and GFP labeled) was assumed. The integrated density of GFP or YFP fluorescence was measured from each imaged cell, and the mean intensity was designated as the fluorescent equivalent of 200 µM actin. Because the ratio of GFP- or YFP-actin/native actin varies on a per cell basis, this allowed for us to internally normalize our GFP- and YFP-actin measurements on a per-cell basis. This also allowed us to directly compare simulated predictions and experimental measurements.

Modeling 2:2:1 and 4:2:1 Nck–N-WASp–Arp2/3 complex binding using Virtual Cell

The Virtual Cell model uses an approximate scheme to describe the binding of N-WASp to the Nck patch and the subsequent activation of Arp2/3 complex. The problem of a single ligand binding to a 2D lattice does not admit exact analytical results because the dependence on ligand size and shape makes the problem intractable. Traditionally, this problem is addressed using approximations for special cases, such as linear ligands or completely symmetric ligands, and by using numerical simulations for more general cases. To our knowledge, no one has described the sequential binding of two ligands to a 2D lattice, as required to describe Arp2/3 complex activation by bound N-WASp. Therefore, we validated our approximations by comparing them with exact numerical simulations for both the 2:2:1 model and the 4:2:1 model. The approximations are considered acceptable if they reproduce the equilibrium values of certain parameters (bound N-WASp, number of N-WASp binding sites, etc.) to reasonable accuracy. In all calculations and simulations, we assume that cytosolic N-WASp, W, and cytosolic Arp2/3 complex A are buffered. This is reasonable based on the volume of the cytosol compared with the size of the patch, and the Virtual Cell simulations show this is an excellent approximation.

2:2:1 model: Virtual Cell approximation. A free Nck site is denoted by N. Then, the 2:2:1 reaction scheme is given by

$$N + W \rightleftharpoons W^* \text{ and}$$

$$S + A \rightleftharpoons A^*,$$

where W^* denotes active N-WASp, A^* denotes active Arp2/3 complex, and S denotes an Arp2/3 complex binding site. In equilibrium, we have

$$NW = K_W W^* \text{ and}$$

$$SA = K_A A^*,$$

where K_W is the dissociation constant for N-WASp, and K_A is an effective dissociation constant for the Arp2/3 complex, which includes both direct dissociation and dissociation via the branching reaction. These equations are supplemented with the conservation of Nck sites, shown as

$$N_{tot} = N + W^* + 2A^*.$$

It will help to introduce a variable describing the number of active N-WASp molecules in the limit $A = 0$, shown as

$$\frac{W_0^*}{N_{tot}} = \frac{W}{K_W + W},$$

which is a known quantity because W is buffered, and K_W is known.

In Virtual Cell, we made the approximation that the number of Arp2/3 complex binding sites is given by

$$S = \beta \frac{N_{tot}}{2}\left(\frac{W^*}{N_{tot}}\right)^2,$$

where β is a prefactor to account for the weight of Arp2/3 complex binding to sites between antibody-induced dimers. In a 1D model, this prefactor is shown as

$$\beta = 1 + \left(\frac{N_{tot} - 2}{N_{tot}}\right)\omega,$$

where $0 \le \omega \le 1$ and $\omega = 0$ if the Arp2/3 complex cannot bind between antibody-induced dimers and $\omega = 1$ if interdimer binding is as likely as intradimer binding. Notice as $N_{tot} \to \infty$, $\beta \to 1 + \omega$, which says that each dimer contributes $1 + \omega$ Arp2/3 complex binding sites. For an infinite 2D hexagonal lattice, we modeled $\beta = 1 + 5\omega$, which accounts for the fact that each Nck site has one pair in the dimer and five neighboring sites where interdimer binding can occur.

We now solve for the equilibrium value of W^* and find that

$$\frac{W^*}{N_{tot}} = \frac{1}{2\beta}\left(\frac{N_{tot}}{W_0^*}\right)\left(\frac{K_A}{A}\right)\left[\sqrt{1 + 4\beta\left(\frac{A}{K_A}\right)\left(\frac{W_0^*}{N_{tot}}\right)^2} - 1\right].$$

In our system, we have $W = 0.05$ µM and $K_W = 0.081$ µM, which gives $W_0^*/N_{tot} = 0.38$.

The concentration of cytosolic Arp2/3 complex is $A = 1.0$ µM. The effective dissociation constant is given by

$$K_A = \frac{k_{off} + k_{branch}}{k_{on}},$$

where k_{on} and k_{off} are the association and dissociation rates of Arp2/3 complex binding, respectively, and k_{branch} is an effective first-order rate constant for the branching reaction, which is proportional to the cytosolic concentrations of F-actin, G-actin, and profilin–G-actin. We assume that

all cytosolic species are buffered, in which case k_{branch} is a well-defined constant giving the branching flux in terms of the concentration of active Arp2/3 complex, $J_{branch} = k_{branch}A^*$. The Virtual Cell simulations give $A^* \approx 200$ molecules/μm^2 and $J_{branch} \approx 3{,}000$ (molecules/μm^2)/s, from which we estimate $k_{branch} \approx 15\ s^{-1}$, and, thus, $K_A \approx 15\ \mu M$. From this, we estimate $A/K_A \approx 0.07$, which shows that the levels of cytosolic Arp2/3 complex are indeed small. To compare with the exact lattice models, it will help to expand the Virtual Cell results in this small parameter. We get

$$\frac{W^*_{VCell}}{N_{tot}} = \frac{W_0^*}{N_{tot}}\left[1-\beta\left(\frac{A}{K_A}\right)\left(\frac{W_0^*}{N_{tot}}\right)^2+2\beta^2\left(\frac{A}{K_A}\right)^2\left(\frac{W_0^*}{N_{tot}}\right)^4\right] \text{ and}$$

$$\frac{S_{VCell}}{N_{tot}} = \beta\frac{1}{2}\left(\frac{W_0^*}{N_{tot}}\right)^2\left[1-2\beta\left(\frac{A}{K_A}\right)\left(\frac{W_0^*}{N_{tot}}\right)^2+5\beta^2\left(\frac{A}{K_A}\right)^2\left(\frac{W_0^*}{N_{tot}}\right)^4\right].$$

Notice that the corrections go as

$$\left(\frac{A}{K_A}\right)\left(\frac{W_0^*}{N_{tot}}\right)^2 \approx 0.027,$$

which is indeed a small parameter.

2D lattice models. For simplicity, we will consider square lattices instead of the hexagonal lattices considered in the text. Square lattices require a different value for the prefactor β but do not change any essential features of the problem. If we consider an $M \times M$ square lattice, then

$$\beta = 1+\frac{3M-4}{M}\omega,$$

with $\beta = 1 + 3\omega$ in the infinite patch limit. Here, we will find analytic solutions for the 2 × 2 lattice and then investigate larger lattices numerically.

Exact results for 2 × 2 patch. A complete model of N-WASp and Arp2/3 complex binding to a 2 × 2 patch requires 15 species, corresponding to a single bound N-WASp, two bound N-WASp molecules, etc., and has $\beta = 1 + \omega$. In steady state, we find

$$\frac{W^*_{2x2}}{N_{tot}} = \left(\frac{W_0^*}{N_{tot}}\right)\frac{1+\beta(A/K_A)\left(W_0^*/N_{tot}\right)^2}{1+2\beta(A/K_A)\left(W_0^*/N_{tot}\right)^2+\beta(A/K_A)^2\left(W_0^*/N_{tot}\right)^4}$$

and

$$\frac{S_{2x2}}{N_{tot}} = \frac{\beta}{2}\left(\frac{W_0^*}{N_{tot}}\right)^2\frac{1+(A/K_A)\left(W_0^*/N_{tot}\right)^2}{1+2\beta(A/K_A)\left(W_0^*/N_{tot}\right)^2+\beta(A/K_A)^2\left(W_0^*/N_{tot}\right)^4},$$

which we expand for small A/K_A to get

$$\frac{W^*_{2x2}}{N_{tot}} = \left(\frac{W_0^*}{N_{tot}}\right)\left[1-\beta\left(\frac{A}{K_A}\right)\left(\frac{W_0^*}{N_{tot}}\right)^2+\beta(2\beta-1)\left(\frac{A}{K_A}\right)^2\left(\frac{W_0^*}{N_{tot}}\right)^4\right] \text{ and}$$

$$\frac{S_{2x2}}{N_{tot}} = \frac{\beta}{2}\left(\frac{W_0^*}{N_{tot}}\right)^2\left[1-(2\beta-1)\left(\frac{A}{K_A}\right)\left(\frac{W_0^*}{N_{tot}}\right)^2+\beta(4\beta-3)\left(\frac{A}{K_A}\right)^2\left(\frac{W_0^*}{N_{tot}}\right)^4\right].$$

Direct comparison to the Virtual Cell approximation gives

$$\frac{W^*_{VCell}}{W^*_{2x2}} = 1+\beta\left(\frac{A}{K_A}\right)^2\left(\frac{W_0^*}{N_{tot}}\right)^4 \approx 1.001 \text{ and}$$

$$\frac{S_{VCell}}{S_{2x2}} = 1-\left(\frac{A}{K_A}\right)\left(\frac{W_0^*}{N_{tot}}\right)^2 \approx 0.97,$$

which shows that the Virtual Cell approximation predicts the total amount of activated N-WASp to better than 1% and the total number of available Arp2/3 complex binding sites to ~3%.

Numerical studies of larger 2D lattices. For simplicity, we work in the $\omega = 1$ limit (recall that $\omega = 0$ corresponds to an ensemble of noninteracting dimers; thus, the 2D structure of the patch has its largest effect when $\omega = 1$). We simulate the binding of N-WASp and Arp2/3 complex to a 30 × 30 Nck lattice at varying Nck densities. In Fig. S4 A, we plot equilibrium-activated N-WASp and the total number of Arp2/3 complex binding sites as a function of cytosolic Arp2/3 complex for 100% Nck density. The Virtual Cell approximation is seen to be in excellent agreement for all Arp2/3 complex concentrations. In Fig. S4 A, we also plot activated N-WASp and Arp2/3 complex binding sites as a function of Nck density for the fixed value $A/K_A = 0.07$ used in our Virtual Cell simulations. The Virtual Cell expression is seen to provide an excellent approximation to the exact numerical results for all densities.

4:2:1 model: Virtual Cell approximation. The 4:2:1 reaction scheme is

$$W + S_W \rightleftharpoons W^* \text{ and}$$

$$A + S_A \rightleftharpoons A^*,$$

where S_W is an N-WASp binding site composed of two adjacent, free Nck molecules, and S_A is an Arp2/3 complex binding site composed of two adjacent, activated N-WASp proteins. In equilibrium, we have

$$S_W W = K_W W^* \text{ and}$$

$$S_A A = K_A A^*,$$

where, as previously described, K_A is an effective dissociation constant, which includes both direct dissociation and dissociation through the branching reaction.

In the 2:2:1 scheme, N-WASp binding was described exactly, and we used an approximate expression giving S_A in terms of W^* and A^*. In the 4:2:1 scheme, we must use approximations for both S_W and S_A, and, therefore, we expect a larger discrepancy between the Virtual Cell approximation and the exact simulations.

In our Virtual Cell model, we approximate

$$S_w = N_{max}\frac{\beta_w}{2}\left(\frac{N}{N_{max}}\right)^2\frac{1}{1-3\left(\frac{A^*}{N_{max}}\right)-\left(\frac{W^*}{N_{max}}\right)} \text{ and}$$

$$S_A = N_{max}\frac{\beta_A}{4}\left(\frac{2W^*}{N_{max}}\right)^2\frac{1}{1-3\left(\frac{A^*}{N_{max}}\right)-\left(\frac{W^*}{N_{max}}\right)},$$

which are only strictly correct for an infinite 1D lattice at 100% Nck density. These equations may be derived by a straightforward extension of the McGhee–von Hippel analysis for binding of a single ligand (McGhee and von Hippel, 1974). Analytical solutions for W^* and A^* may be obtained with these formulae, but these are complicated and not particularly enlightening.

Instead, we will directly compare the Virtual Cell results to the results from numerical simulations.

Exact numerical results. We simulated the 4:2:1 model using a 30 × 30 square lattice at varying Nck densities. In Fig. S4 B, we plot S_W, W^*, S_A, and A^* as a function of Nck density using the same cytosolic concentrations and dissociation constants as previously described. The Virtual Cell approximation consistently underestimates N-WASp binding sites and activated N-WASp by ∼20–30%, whereas it consistently overestimates Arp2/3 complex binding sites and bound Arp2/3 complex by about the same amount. However, note that bound Arp2/3 complex, which is the important output of this scheme, is usually within the error bars of the stochastic simulations. Moreover, the Virtual Cell approximation faithfully captures the variations in these curves as the density is varied; that is, the Virtual Cell approximation overestimates the actual values by the same fractional amount at each density. This tells us that the shapes of our curves will be accurate, even if the exact values are not. Overall, the approximation provides sufficient accuracy and is more than adequate to distinguish between the 2:2:1 model and the 4:2:1 model.

WIP KO studies

WIP WT and KO MEFs were provided by N. Ramesh and R. Geha (Children's Hospital, Boston, MA). Both cell types were grown in high-glucose DME containing 15% FCS and 1% penicillin-streptomycin. EBB CD16-7–Nck SH3 (1+2+3)–HA and pmCherry–actin C1 as well as CB6 GFP-WIP (provided by M. Way, London Research Institute, London, England, UK) in WIP rescue experiments were transfected into MEFs using Lipofectamine reagent. CD16-7–mCherry–Nck SH3–HA was aggregated using anti-CD16 antibody and goat anti–mouse Alexa Fluor 488 or 647 (Invitrogen). Images were obtained using a confocal microscope (LSM 780) with a 63× 1.4 NA oil immersion objective.

WIP and N-WASp recruitment studies

WIP WT and KO MEFs were grown in high-glucose DMEM containing 15% FCS and 1% penicillin-streptomycin. N-WASp WT and KO MEFs were grown in high-glucose DME containing 10% FCS and 1% penicillin-streptomycin. EBB CD16-7–Nck SH3 1+2+3, pmCherry–actin C1, and CB6 GFP-WIP or CB6 GFP–N-WASp (provided by M. Way) were transfected into MEFs using Lipofectamine reagent. CD16-7–Nck SH3–HA was aggregated using anti-CD16 antibody and goat anti–mouse Alexa Fluor 647. Cells were fixed using 4% PFA (Electron Microscopy Sciences) and mounted on slides using Fluoromount-G (SouthernBiotech). Images were obtained using a confocal microscope (LSM 780) with a 63× 1.4 NA oil immersion objective using ZEN image acquisition software.

For mixed Nck SH3 domain aggregates, NIH-3T3 fibroblasts were transfected with a mixture of EBB CD16-7–Nck SH3 1, EBB CD16-7–Nck SH3 2, EBB CD16-7–Nck 1+2+3, and/or EBB CD16-7 (dummy), CB6 GFP–N-WASp, and pmCherry–actin C1 and cells analyzed as previously outlined.

Statistical analysis

All statistical analysis was performed using the SPSS program (IBM). Correlations of aggregate properties and actin comet tail properties were determined using Pearson's correlation. Statistical significance among actin comet tail characteristics in different Nck aggregate density groups was determined using analysis of variance with a post-hoc Tukey's test.

Online supplemental material

Fig. S1 contains information that describes the methods used for CD16-7 fusion protein aggregation, the fusion proteins used in the experiments, and Western blots demonstrating the expression of CD16-7–mCherry–Nck SH3–HA versus CD16-7–dummy-HA or endogenous Nck. Fig. S2 supports the quantitative data presented in Fig. 1, comparing either the number of Nck SH3 molecules in aggregates or the velocity of Nck SH3 aggregates with measured characteristics of actin comet tails. Fig. S3 shows that Nck SH3 aggregates containing both Nck SH3 (2) and Nck SH3 (1+2+3) induce actin polymerization in a manner similar to 100% Nck SH3 (1+2+3) aggregates, whereas aggregates composed of 50% Nck SH3 (1+2+3) or 100% Nck SH3 (2) do not induce actin comet tail formation. Fig. S4 shows that the approximations describing N-WASp or Arp2/3 complex binding at Nck SH3 aggregates is sufficiently accurate, when compared with exact numerical calculations, to describe binding of N-WASp to Nck or Arp2/3 complex to N-WASp and actin polymerization downstream of Arp2/3 complex activation. Video 1 compliments Fig. 1 by showing a time-lapse image of two Nck SH3 aggregates being pushed across the membrane by polymerizing actin comet tails. Video 2 compliments Fig. 3 by showing time-lapse images of cells containing aggregates composed of 0–100% Nck SH3 domains. Video 3 compliments Fig. 6 by showing time-lapse images of Nck aggregates in WIP KO, WT, or GFP-WIP–rescued KO MEFs, demonstrating the necessity of WIP in Nck-induced actin polymerization. Table S1 contains data demonstrating that quenching of mCherry fluorescence is not caused by aggregation of labeled Nck SH3 fusion proteins. Table S2 lists protein names and descriptions used in the Virtual Cell simplified actin dendritic nucleation model. Table S3 lists global parameters. Table S4 contains information describing the reactants and reactions contained in the 1:1:1, 2:2:1, and 4:2:1 Virtual Cell models. Our models are also included in the supplemental materials as XML files: the 1:1:1 model is named Nck Induces Actin Comet Tail Formation Single NWASP Activation of Arp23 Simplified Actin Dendritic Nucleation; the 2:2:1 model is named Nck Induces Actin Comet Tail Formation Dimer NWASP Activation of Arp23 Simplified Actin Dendritic Nucleation; and the 4:2:1 model is named Nck Induces Actin Comet Tail Formation Dimer Nck Binds NWASP With Dimer NWASP Activation of Arp23 Simplified Actin Dendritic Nucleation. Online supplemental material is available at http://www.jcb.org/cgi/content/full/jcb.201111113/DC1.

We thank A. Cowan and S. Krueger for expert advice in imaging techniques and image analysis; M. Way for generously providing GFP-WIP and GFP–N-WASp expression vectors; and R. Geha and N. Ramesh for generously providing WT and KO WIP MEFs.

This work was supported by National Institutes of Health grants from the National Center for Research Resources (2P41RR013186-15) and the National Institute of Diabetes and Digestive and Kidney Diseases (TR01DK087660 to L.M. Loew, 1S10RR019428-01 to W.A. Mohler, and RO1 CA82258 to B.J. Mayer).

Submitted: 23 November 2011
Accepted: 17 April 2012

References

Alberts, J.B., and G.M. Odell. 2004. In silico reconstitution of *Listeria* propulsion exhibits nano-saltation. *PLoS Biol.* 2:e412. http://dx.doi.org/10.1371/journal.pbio.0020412

Antón, I.M., W. Lu, B.J. Mayer, N. Ramesh, and R.S. Geha. 1998. The Wiskott-Aldrich syndrome protein-interacting protein (WIP) binds to the adaptor protein Nck. *J. Biol. Chem.* 273:20992–20995. http://dx.doi.org/10.1074/jbc.273.33.20992

Antón, I.M., M.A. de la Fuente, T.N. Sims, S. Freeman, N. Ramesh, J.H. Hartwig, M.L. Dustin, and R.S. Geha. 2002. WIP deficiency reveals a differential role for WIP and the actin cytoskeleton in T and B cell activation. *Immunity.* 16:193–204. http://dx.doi.org/10.1016/S1074-7613(02)00268-6

Barda-Saad, M., A. Braiman, R. Titerence, S.C. Bunnell, V.A. Barr, and L.E. Samelson. 2005. Dynamic molecular interactions linking the T cell antigen receptor to the actin cytoskeleton. *Nat. Immunol.* 6:80–89. http://dx.doi.org/10.1038/ni1143

Barda-Saad, M., N. Shirasu, M.H. Pauker, N. Hassan, O. Perl, A. Balbo, H. Yamaguchi, J.C. Houtman, E. Appella, P. Schuck, and L.E. Samelson. 2010. Cooperative interactions at the SLP-76 complex are critical for actin polymerization. *EMBO J.* 29:2315–2328. http://dx.doi.org/10.1038/emboj.2010.133

Beltzner, C.C., and T.D. Pollard. 2008. Pathway of actin filament branch formation by Arp2/3 complex. *J. Biol. Chem.* 283:7135–7144. http://dx.doi.org/10.1074/jbc.M705894200

Benesch, S., S. Lommel, A. Steffen, T.E. Stradal, N. Scaplehorn, M. Way, J. Wehland, and K. Rottner. 2002. Phosphatidylinositol 4,5-biphosphate (PIP2)-induced vesicle movement depends on N-WASP and involves Nck, WIP, and Grb2. *J. Biol. Chem.* 277:37771–37776. http://dx.doi.org/10.1074/jbc.M204145200

Bertuccio, C., D. Veron, P.K. Aggarwal, L. Holzman, and A. Tufro. 2011. Vascular endothelial growth factor receptor 2 direct interaction with nephrin links VEGF-A signals to actin in kidney podocytes. *J. Biol. Chem.* 286:39933–39944. http://dx.doi.org/10.1074/jbc.M111.241620

Bindschadler, M., E.A. Osborn, C.F. Dewey Jr., and J.L. McGrath. 2004. A mechanistic model of the actin cycle. *Biophys. J.* 86:2720–2739. http://dx.doi.org/10.1016/S0006-3495(04)74326-X

Bunting, J.R., T.V. Phan, E. Kamali, and R.M. Dowben. 1989. Fluorescent cationic probes of mitochondria. Metrics and mechanism of interaction. *Biophys. J.* 56:979–993. http://dx.doi.org/10.1016/S0006-3495(89)82743-2

Carlier, M.F., P. Nioche, I. Broutin-L'Hermite, R. Boujemaa, C. Le Clainche, C. Egile, C. Garbay, A. Ducruix, P. Sansonetti, and D. Pantaloni. 2000. GRB2 links signaling to actin assembly by enhancing interaction of neural Wiskott-Aldrich syndrome protein (N-WASp) with actin-related protein

(ARP2/3) complex. *J. Biol. Chem.* 275:21946–21952. http://dx.doi.org/10.1074/jbc.M000687200

Carlsson, A.E. 2006. Stimulation of actin polymerization by filament severing. *Biophys. J.* 90:413–422. http://dx.doi.org/10.1529/biophysj.105.069765

Carlsson, A.E., M.A. Wear, and J.A. Cooper. 2004. End versus side branching by Arp2/3 complex. *Biophys. J.* 86:1074–1081. http://dx.doi.org/10.1016/S0006-3495(04)74182-X

Ditlev, J.A., N.M. Vacanti, I.L. Novak, and L.M. Loew. 2009. An open model of actin dendritic nucleation. *Biophys. J.* 96:3529–3542. http://dx.doi.org/10.1016/j.bpj.2009.01.037

dos Remedios, C.G., D. Chhabra, M. Kekic, I.V. Dedova, M. Tsubakihara, D.A. Berry, and N.J. Nosworthy. 2003. Actin binding proteins: Regulation of cytoskeletal microfilaments. *Physiol. Rev.* 83:433–473.

Duchen, M.R., and T.J. Biscoe. 1992. Relative mitochondrial membrane potential and [Ca2+]i in type I cells isolated from the rabbit carotid body. *J. Physiol.* 450:33–61.

Fink, C., F. Morgan, and L.M. Loew. 1998. Intracellular fluorescent probe concentrations by confocal microscopy. *Biophys. J.* 75:1648–1658. http://dx.doi.org/10.1016/S0006-3495(98)77607-6

Frischknecht, F., V. Moreau, S. Röttger, S. Gonfloni, I. Reckmann, G. Superti-Furga, and M. Way. 1999. Actin-based motility of vaccinia virus mimics receptor tyrosine kinase signalling. *Nature*. 401:926–929. http://dx.doi.org/10.1038/44860

Fukuoka, M., S. Suetsugu, H. Miki, K. Fukami, T. Endo, and T. Takenawa. 2001. A novel neural Wiskott-Aldrich syndrome protein (N-WASP) binding protein, WISH, induces Arp2/3 complex activation independent of Cdc42. *J. Cell Biol.* 152:471–482. http://dx.doi.org/10.1083/jcb.152.3.471

Higgs, H.N., and T.D. Pollard. 2000. Activation by Cdc42 and PIP(2) of Wiskott-Aldrich syndrome protein (WASp) stimulates actin nucleation by Arp2/3 complex. *J. Cell Biol.* 150:1311–1320. http://dx.doi.org/10.1083/jcb.150.6.1311

Jones, N., I.M. Blasutig, V. Eremina, J.M. Ruston, F. Bladt, H. Li, H. Huang, L. Larose, S.S. Li, T. Takano, et al. 2006. Nck adaptor proteins link nephrin to the actin cytoskeleton of kidney podocytes. *Nature*. 440:818–823. http://dx.doi.org/10.1038/nature04662

Jones, N., L.A. New, M.A. Fortino, V. Eremina, J. Ruston, I.M. Blasutig, L. Aoudjit, Y. Zou, X. Liu, G.L. Yu, et al. 2009. Nck proteins maintain the adult glomerular filtration barrier. *J. Am. Soc. Nephrol.* 20:1533–1543. http://dx.doi.org/10.1681/ASN.2009010056

Jordan, M.S., J. Sadler, J.E. Austin, L.D. Finkelstein, A.L. Singer, P.L. Schwartzberg, and G.A. Koretzky. 2006. Functional hierarchy of the N-terminal tyrosines of SLP-76. *J. Immunol.* 176:2430–2438.

Kapustina, M., E. Vitriol, T.C. Elston, L.M. Loew, and K. Jacobson. 2010. Modeling capping protein FRAP and CALI experiments reveals in vivo regulation of actin dynamics. *Cytoskeleton (Hoboken)*. 67:519–534.

Lapetina, S., C.C. Mader, K. Machida, B.J. Mayer, and A.J. Koleske. 2009. Arg interacts with cortactin to promote adhesion-dependent cell edge protrusion. *J. Cell Biol.* 185:503–519. http://dx.doi.org/10.1083/jcb.200809085

Mahaffy, R.E., and T.D. Pollard. 2006. Kinetics of the formation and dissociation of actin filament branches mediated by Arp2/3 complex. *Biophys. J.* 91:3519–3528. http://dx.doi.org/10.1529/biophysj.106.080937

McGhee, J.D., and P.H. von Hippel. 1974. Theoretical aspects of DNA-protein interactions: Co-operative and non-co-operative binding of large ligands to a one-dimensional homogeneous lattice. *J. Mol. Biol.* 86:469–489. http://dx.doi.org/10.1016/0022-2836(74)90031-X

McGrath, J.L., N.J. Eungdamrong, C.I. Fisher, F. Peng, L. Mahadevan, T.J. Mitchison, and S.C. Kuo. 2003. The force-velocity relationship for the actin-based motility of *Listeria* monocytogenes. *Curr. Biol.* 13:329–332. http://dx.doi.org/10.1016/S0960-9822(03)00051-4

Michalski, P.J., and A.E. Carlsson. 2010. The effects of filament aging and annealing on a model lamellipodium undergoing disassembly by severing. *Phys. Biol.* 7:026004. http://dx.doi.org/10.1088/1478-3975/7/2/026004

Mogilner, A. 2006. On the edge: Modeling protrusion. *Curr. Opin. Cell Biol.* 18:32–39. http://dx.doi.org/10.1016/j.ceb.2005.11.001

Moreau, V., F. Frischknecht, I. Reckmann, R. Vincentelli, G. Rabut, D. Stewart, and M. Way. 2000. A complex of N-WASP and WIP integrates signalling cascades that lead to actin polymerization. *Nat. Cell Biol.* 2:441–448. http://dx.doi.org/10.1038/35017080

Novak, I.L., B.M. Slepchenko, and A. Mogilner. 2008. Quantitative analysis of G-actin transport in motile cells. *Biophys. J.* 95:1627–1638. http://dx.doi.org/10.1529/biophysj.108.130096

Oser, M., C.C. Mader, H. Gil-Henn, M. Magalhaes, J.J. Bravo-Cordero, A.J. Koleske, and J. Condeelis. 2010. Specific tyrosine phosphorylation sites on cortactin regulate Nck1-dependent actin polymerization in invadopodia. *J. Cell Sci.* 123:3662–3673. http://dx.doi.org/10.1242/jcs.068163

Oser, M., A. Dovas, D. Cox, and J. Condeelis. 2011. Nck1 and Grb2 localization patterns can distinguish invadopodia from podosomes. *Eur. J. Cell Biol.* 90:181–188. http://dx.doi.org/10.1016/j.ejcb.2010.08.006

Padrick, S.B., and M.K. Rosen. 2010. Physical mechanisms of signal integration by WASP family proteins. *Annu. Rev. Biochem.* 79:707–735. http://dx.doi.org/10.1146/annurev.biochem.77.060407.135452

Padrick, S.B., H.C. Cheng, A.M. Ismail, S.C. Panchal, L.K. Doolittle, S. Kim, B.M. Skehan, J. Umetani, C.A. Brautigam, J.M. Leong, and M.K. Rosen. 2008. Hierarchical regulation of WASP/WAVE proteins. *Mol. Cell*. 32:426–438. http://dx.doi.org/10.1016/j.molcel.2008.10.012

Padrick, S.B., L.K. Doolittle, C.A. Brautigam, D.S. King, and M.K. Rosen. 2011. Arp2/3 complex is bound and activated by two WASP proteins. *Proc. Natl. Acad. Sci. USA*. 108:E472–E479. http://dx.doi.org/10.1073/pnas.1100236108

Papayannopoulos, V., C. Co, K.E. Prehoda, S. Snapper, J. Taunton, and W.A. Lim. 2005. A polybasic motif allows N-WASP to act as a sensor of PIP(2) density. *Mol. Cell*. 17:181–191. http://dx.doi.org/10.1016/j.molcel.2004.11.054

Pauker, M.H., and M. Barda-Saad. 2011. Studies of novel interactions between Nck and VAV SH3 domains. *Commun Integr Biol*. 4:175–177. http://dx.doi.org/10.4161/cib.4.2.14235

Pawson, T. 2004. Specificity in signal transduction: From phosphotyrosine-SH2 domain interactions to complex cellular systems. *Cell*. 116:191–203. http://dx.doi.org/10.1016/S0092-8674(03)01077-8

Pollard, T.D. 2007. Regulation of actin filament assembly by Arp2/3 complex and formins. *Annu. Rev. Biophys. Biomol. Struct.* 36:451–477. http://dx.doi.org/10.1146/annurev.biophys.35.040405.101936

Pollard, T.D., and G.G. Borisy. 2003. Cellular motility driven by assembly and disassembly of actin filaments. *Cell*. 112:453–465. http://dx.doi.org/10.1016/S0092-8674(03)00120-X

Prehoda, K.E., J.A. Scott, R.D. Mullins, and W.A. Lim. 2000. Integration of multiple signals through cooperative regulation of the N-WASP-Arp2/3 complex. *Science*. 290:801–806. http://dx.doi.org/10.1126/science.290.5492.801

Rajmohan, R., A. Raodah, M.H. Wong, and T. Thanabalu. 2009. Characterization of Wiskott-Aldrich syndrome (WAS) mutants using *Saccharomyces cerevisiae*. *FEM. Yeast Res.* 9:1226–1235. http://dx.doi.org/10.1111/j.1567-1364.2009.00581.x

Rao, Y. 2005. Dissecting Nck/Dock signaling pathways in *Drosophila* visual system. *Int. J. Biol. Sci.* 1:80–86. http://dx.doi.org/10.7150/ijbs.1.80

Rao, Y., and S.L. Zipursky. 1998. Domain requirements for the Dock adapter protein in growth- cone signaling. *Proc. Natl. Acad. Sci. USA*. 95:2077–2082. http://dx.doi.org/10.1073/pnas.95.5.2077

Rivera, G.M., C.A. Briceño, F. Takeshima, S.B. Snapper, and B.J. Mayer. 2004. Inducible clustering of membrane-targeted SH3 domains of the adaptor protein Nck triggers localized actin polymerization. *Curr. Biol.* 14:11–22. http://dx.doi.org/10.1016/j.cub.2003.12.033

Rivera, G.M., S. Antoku, S. Gelkop, N.Y. Shin, S.K. Hanks, T. Pawson, and B.J. Mayer. 2006. Requirement of Nck adaptors for actin dynamics and cell migration stimulated by platelet-derived growth factor B. *Proc. Natl. Acad. Sci. USA*. 103:9536–9541. http://dx.doi.org/10.1073/pnas.0603786103

Rivera, G.M., D. Vasilescu, V. Papayannopoulos, W.A. Lim, and B.J. Mayer. 2009. A reciprocal interdependence between Nck and PI(4,5)P(2) promotes localized N-WASp-mediated actin polymerization in living cells. *Mol. Cell*. 36:525–535. http://dx.doi.org/10.1016/j.molcel.2009.10.025

Rohatgi, R., P. Nollau, H.Y. Ho, M.W. Kirschner, and B.J. Mayer. 2001. Nck and phosphatidylinositol 4,5-bisphosphate synergistically activate actin polymerization through the N-WASP-Arp2/3 pathway. *J. Biol. Chem.* 276:26448–26452. http://dx.doi.org/10.1074/jbc.M103856200

Rong, S.B., and M. Vihinen. 2000. Structural basis of Wiskott-Aldrich syndrome causing mutations in the WH1 domain. *J. Mol. Med.* 78:530–537. http://dx.doi.org/10.1007/s001090000136

Sallee, N.A., G.M. Rivera, J.E. Dueber, D. Vasilescu, R.D. Mullins, B.J. Mayer, and W.A. Lim. 2008. The pathogen protein EspF(U) hijacks actin polymerization using mimicry and multivalency. *Nature*. 454:1005–1008. http://dx.doi.org/10.1038/nature07170

Sasahara, Y., R. Rachid, M.J. Byrne, M.A. de la Fuente, R.T. Abraham, N. Ramesh, and R.S. Geha. 2002. Mechanism of recruitment of WASP to the immunological synapse and of its activation following TCR ligation. *Mol. Cell*. 10:1269–1281. http://dx.doi.org/10.1016/S1097-2765(02)00728-1

Scaplehorn, N., A. Holmström, V. Moreau, F. Frischknecht, I. Reckmann, and M. Way. 2002. Grb2 and Nck act cooperatively to promote actin-based motility of vaccinia virus. *Curr. Biol.* 12:740–745. http://dx.doi.org/10.1016/S0960-9822(02)00812-6

Sondermann, P., R. Huber, V. Oosthuizen, and U. Jacob. 2000. The 3.2-A crystal structure of the human IgG1 Fc fragment-Fc gammaRIII complex. *Nature*. 406:267–273. http://dx.doi.org/10.1038/35018508

Stewart, D.M., L. Tian, and D.L. Nelson. 1999. Mutations that cause the Wiskott-Aldrich syndrome impair the interaction of Wiskott-Aldrich syndrome protein (WASP) with WASP interacting protein. *J. Immunol.* 162:5019–5024.

Stylli, S.S., T.T. Stacey, A.M. Verhagen, S.S. Xu, I. Pass, S.A. Courtneidge, and P. Lock. 2009. Nck adaptor proteins link Tks5 to invadopodia actin regulation and ECM degradation. *J. Cell Sci.* 122:2727–2740. http://dx.doi.org/10.1242/jcs.046680

Tehrani, S., N. Tomasevic, S. Weed, R. Sakowicz, and J.A. Cooper. 2007. Src phosphorylation of cortactin enhances actin assembly. *Proc. Natl. Acad. Sci. USA*. 104:11933–11938. http://dx.doi.org/10.1073/pnas.0701077104

Ti, S.C., C.T. Jurgenson, B.J. Nolen, and T.D. Pollard. 2011. Structural and biochemical characterization of two binding sites for nucleation-promoting factor WASp-VCA on Arp2/3 complex. *Proc. Natl. Acad. Sci. USA*. 108: E463–E471. http://dx.doi.org/10.1073/pnas.1100125108

Verma, R., I. Kovari, A. Soofi, D. Nihalani, K. Patrie, and L.B. Holzman. 2006. Nephrin ectodomain engagement results in Src kinase activation, nephrin phosphorylation, Nck recruitment, and actin polymerization. *J. Clin. Invest.* 116:1346–1359. http://dx.doi.org/10.1172/JCI27414

Weisswange, I., T.P. Newsome, S. Schleich, and M. Way. 2009. The rate of N-WASP exchange limits the extent of ARP2/3-complex-dependent actin-based motility. *Nature*. 458:87–91. http://dx.doi.org/10.1038/nature07773

Wiesner, S., E. Helfer, D. Didry, G. Ducouret, F. Lafuma, M.F. Carlier, and D. Pantaloni. 2003. A biomimetic motility assay provides insight into the mechanism of actin-based motility. *J. Cell Biol.* 160:387–398. http://dx.doi.org/10.1083/jcb.200207148

Wu, J.Q., and T.D. Pollard. 2005. Counting cytokinesis proteins globally and locally in fission yeast. *Science*. 310:310–314. http://dx.doi.org/10.1126/science.1113230

Yamaguchi, H., M. Lorenz, S. Kempiak, C. Sarmiento, S. Coniglio, M. Symons, J. Segall, R. Eddy, H. Miki, T. Takenawa, and J. Condeelis. 2005. Molecular mechanisms of invadopodium formation: The role of the N-WASP–Arp2/3 complex pathway and cofilin. *J. Cell Biol.* 168:441–452. http://dx.doi.org/10.1083/jcb.200407076